Chapter 10.   Phase Transformations in Solids

10.1 Introduction

A solid system of a given composition can exist in a variety of chemical and crystallographic arrangements or *phases*. A phase is defined as a homogeneous region in a liquid or a solid, with a characteristic atomic arrangement and chemical composition[1]. Depending on the *thermodynamic variables* (temperature, pressure, chemical composition) different phases or mixtures of phases are stable (the *equilibrium state*). Phase stability and phase transformations are crucial to the design, behavior, and overall performance of all materials, including metals and ceramics. This chapter deals with the criteria for *phase stability* and with the processes of *phase transformations* in condensed matter.

Phase transformations follow the principle of minimization of Gibbs energy. This means the equilibrium product is always the combination of phases and compositions that minimizes the overall Gibbs energy of the system for a particular set of thermodynamic variables. This final state would only be attained in an infinite amount of time, and heat treatments of real materials stop short of reducing the Gibbs energy to its absolute minimum value. However, the overall trends of phase transformations follow the tendencies established by thermodynamics.

The most stable state of a crystalline solid would be a single crystal with a small concentration of defects (see Chapter 4). This is a very difficult state to attain and most solids contain a certain proportion of lattice defects, including point defects, dislocations, and grain boundaries. Although heat treatments do not eliminate all dislocations, their density is reduced, with an attendant decrease in material hardness. Similar control is possible with other microstructural features such as grain size, precipitate size and density, etc. Materials can be fabricated with a variety of microstructures which yield a range of the macroscopic properties of interest. The mechanisms of phase transformations affect the performance of materials used in nuclear power, both in the as-fabricated state and during irradiation, as described in this Chapter and Chapter 24.

The thermodynamics of phase transformations are reviewed first, followed by discussions of (i) the processes by which the transformations take place, from nucleation and growth to spinodal phase transitions and (ii) the use of such knowledge to produce microstructures with favorable macroscopic properties through thermo-mechanical processing. The chapter ends with a discussion of order-disorder and amorphization phase transitions.
.

10.2. Thermodynamics of Phase Changes[2]

10.2.1 Driving Force for Phase Transformations

---

[1] Only *condensed* phases (liquids and solids) are considered. A gas phase is always present, but is ignored when dealing with condensed-phase equilibria.

[2] See also Sects. 2.5 and 2.6

As described in Chap. 2, the driving force for phase transformations is the minimization of the Gibbs energy *g*. For one mole of a pure substance or a mixture:

$$g = h - Ts \qquad (10.1)$$

where h is the molar enthalpy, s is the molar entropy and T is temperature. Phase transformations occur in the direction of decreasing Gibbs energy, such that if a lower Gibbs energy state is available, a driving force exists to transform the system to this state. As a consequence, the equilibrium state is achieved when the derivative of the Gibbs energy with respect to all possible changes in a given parameter X, such as composition or pressure, is zero (Sect. 2.4).

$$\left(\frac{dg}{dX} \right) = 0 \qquad (10.2)$$

The above condition is attained when the Gibbs energy is a minimum. Temperature is a common variable that affects phase stability. Figure 10.1 shows schematically the variation of the Gibbs energy for the solid and liquid phases near the melting point (T_m). Sol_1 and Sol_2 have different crystal structures.
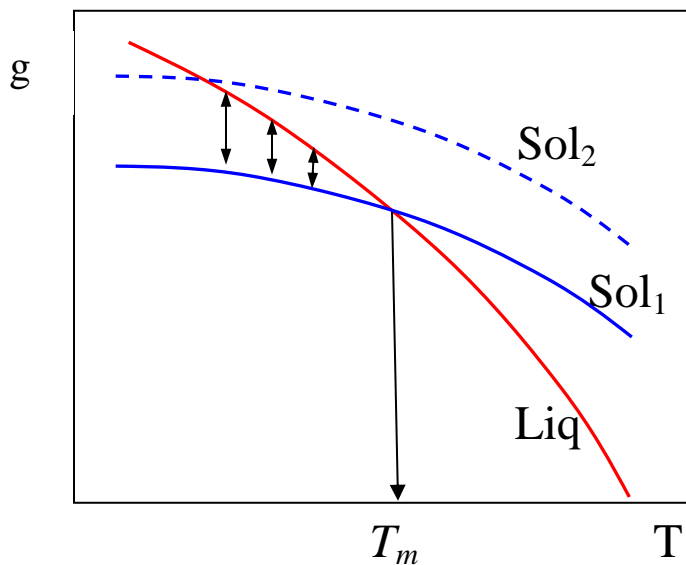
Figure 10 1 Schematic plot of the Gibbs energy of the liquid (Liq) and two solid phases in a single-component system.

At $T > T_m$ the Gibbs energy of the liquid phase Liq (red curve) is lower than that of the solid phase Sol_1 (blue curve) which means the liquid is the most stable phase. As the temperature is decreased, the Gibbs energy difference between the two phases decreases, such that at the melting temperature, the two have the same Gibbs energy. Reducing the temperature below T_m causes the Sol_1 to become the most stable phase, thereby creating a

driving force for solidification. In principle there are many possible solid phases, (e.g. the Sol$_2$ phase shown in Fig.10.1), but they have higher Gibbs energies than the stable solid and so they form only as metastable phases.

As the temperature increases the value of g changes because of increasing entropy. From Eq 2.16:

$$\left(\frac{\partial g}{\partial T}\right)_p = -s \tag{10.3}$$

Thus, as the temperature increases, phases with larger molar entropy tend to be favored over lower-entropy phases. This is one of the reasons why liquids, whose atomic configuration is more disordered than that of solids, become more stable than solids at high temperature.

As indicated in Eq (10.3), the total pressure p is a thermodynamic variable. However, the Gibbs energies of condensed phases are largely insensitive to pressure because their molar volumes v are very small, and from Eq (2.16):

$$\left(\frac{\partial g}{\partial p}\right)_T = v \tag{10.4}$$

10.2.2. Phase Diagrams and Gibbs energy curves

Phase diagrams are maps (for solids most often of temperature vs. composition) indicating which phases are present at equilibrium for the given conditions (temperature and composition). In principle, phase diagrams can be deduced if the Gibbs energy-composition curves at various temperatures are known for all the possible phases in the system. If the thermodynamic quantities that are used to calculate the Gibbs energy are known experimentally, the phase diagrams can be calculated [1].

In practice, phase diagrams often originate from empirical data. Different mixtures of the components of the system are produced, and at various temperatures, the phases present are determined by x-ray diffraction and chemical analysis. Although most solids contain more than two components, for simplicity only binary phase diagrams will be studied in this chapter. However, understanding of ternary and higher- order phase diagrams can help guide the design of more complex systems.

Figure 10.1 demonstrated how the minimum Gibbs energy of a pure component (or a mixture of fixed composition) is achieved as temperature is varied. In this section, the variables are switched: temperature and overall composition of an A-B binary system are held constant but the phases present and their compositions are determined by minimizing the total Gibbs energy.

Figure 10.2 shows a plot of Gibbs energy versus composition for a binary system A-B showing Gibbs energy curves for two phases: alpha and beta. The Gibbs energy of the alpha phase shows a minimum in the A-rich region and the beta phase shows a minimum in the B-rich region. The Gibbs energy curve for the liquid is higher than that of either solid phase. According to Figure 10.2, in the A-rich region, the stable phase is single-phase alpha while in the B-rich region the stable phase is single-phase beta. In the in-between region, for example at the point x_o, the lowest Gibbs energy curve is that of the alpha phase. This would indicate that single-phase alpha with composition x_o would be observed. However as shown below, $\alpha(x_o)$ is unstable with respect to a combination of alpha and beta at slightly different compositions. Then the B content of the alpha phase will decrease to form the beta phase and it is possible to reach compositions x_1 and x_2. In that case the overall Gibbs energy can be written:

$$g_{3'} = M_\alpha g_{1'} + M_\beta g_{2'} \qquad (10.5)$$

where M_α, M_β are the mole fractions of alpha and beta, and $g_{1'}$ and $g_{2'}$ the molar Gibbs energy of alpha at composition $x_{1'}$ and beta at composition $x_{2'}$, respectively. Since

$$M_\alpha + M_\beta = 1 \qquad (10.6)$$

it is clear that the Gibbs energy of the alpha-beta mixture will be a linear combination of the Gibbs energies of the two phases and therefore will lie on the line g_1 - g_2. Using the *lever rule*

$$g_{3'} = \frac{(x_o - x_{1'})}{(x_{2'} - x_{1'})} g_{2'} + \frac{(x_{2'} - x_o)}{(x_{2'} - x_{1'})} g_{1'} \qquad (10.7)$$

Thus, since $g_{3'}$ lies on the line g_1 - g_2 and is at composition x_o it is lower than g_o. As a result, the single-phase alpha phase at composition x_o is unstable with respect to the mixture of alpha at composition $x_{1'}$ and beta at composition $x_{2'}$. This creates a driving force for the beta phase beta to nucleate and for B atoms to transfer from alpha to beta.

This process continues until the compositions x_1 and x_2 are reached. A mixture of alpha at x_1 and beta at x_2 provides the lowest overall Gibbs energy g_3 that can be achieved for the binary alloy shown in Figure 10.2 at composition x_o. The points x_1 and x_2 are found by taking the common tangent of the α and β Gibbs energy curves. For compositions in between the two, it is favorable for a second phase (beta) to form by precipitation . For $x < x_1$, or $x > x_2$ single phase alpha and beta respectively are seen.

We should note that for the two coexisting phases at compositions x_1 and x_2, the chemical potential of *A* and *B* atoms in the alpha and beta phases is the same. If x corresponds to the content of B in a binary solution, then (see chapter 2),

$$\left.\frac{dg_\alpha}{dx}\right|_{x_1} = \mu_B^\alpha \; ; \; \left.\frac{dg_\beta}{dx}\right|_{x_2} = \mu_B^\beta \; \text{ and } \; \mu_B^\alpha = \mu_B^\beta \tag{10.8}$$

That means that there is no driving force for a B atom in either phase to move to the other, (since its chemical potential is identical in the two phases) which means the system is *at equilibrium.*

The net result is that at a given temperature the equilibrium phases are those that would be predicted by the lower envelope of the possible Gibbs energy curves, if it is considered that such envelope contains the common tangents such as $g_1 - g_2$ shown in Figure 10.2.
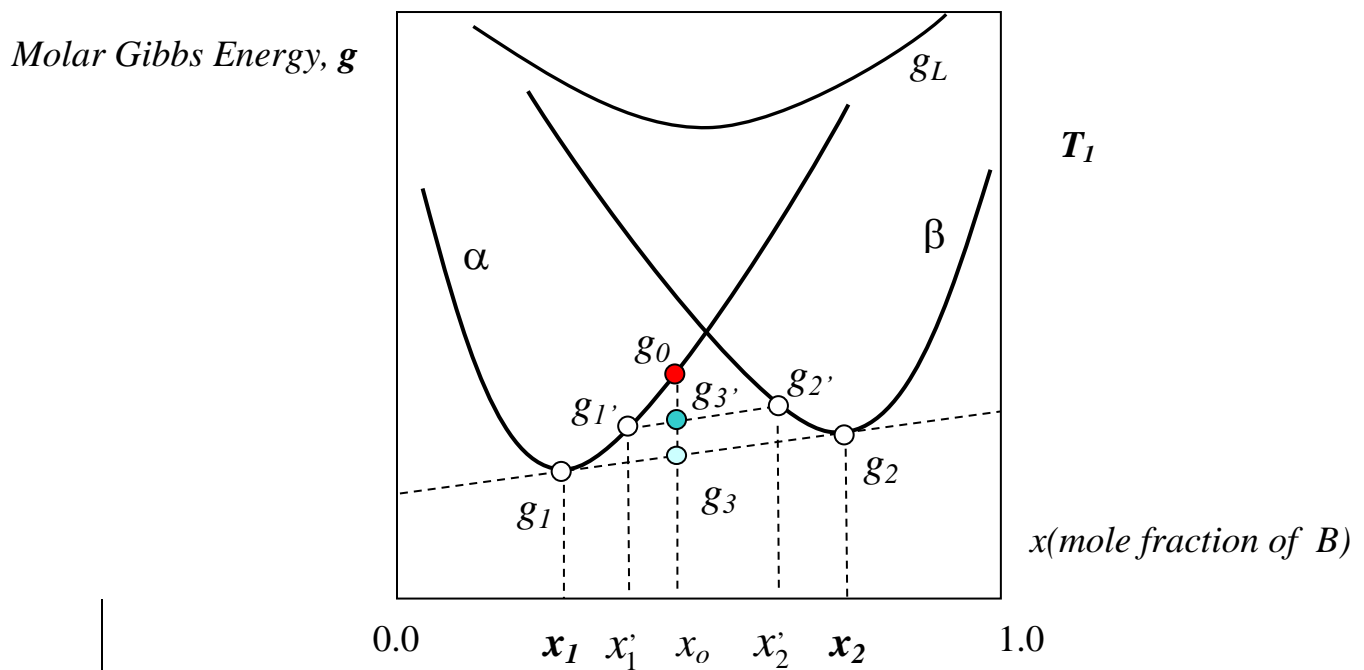
Fig. 10.2 Molar Gibbs energy curves for the α and β phases of the A-B binary system at temperature T_1

The above derivation allows us to relate the Gibbs energy variation with composition to the Gibbs energy-composition phase diagram. In Figure 10.2, which was sketched for a fixed temperature, the single alpha stability domain ranges from 0 to x_1 the two-phase domain from x_1 to x_2 and single beta from x_2 to 1.
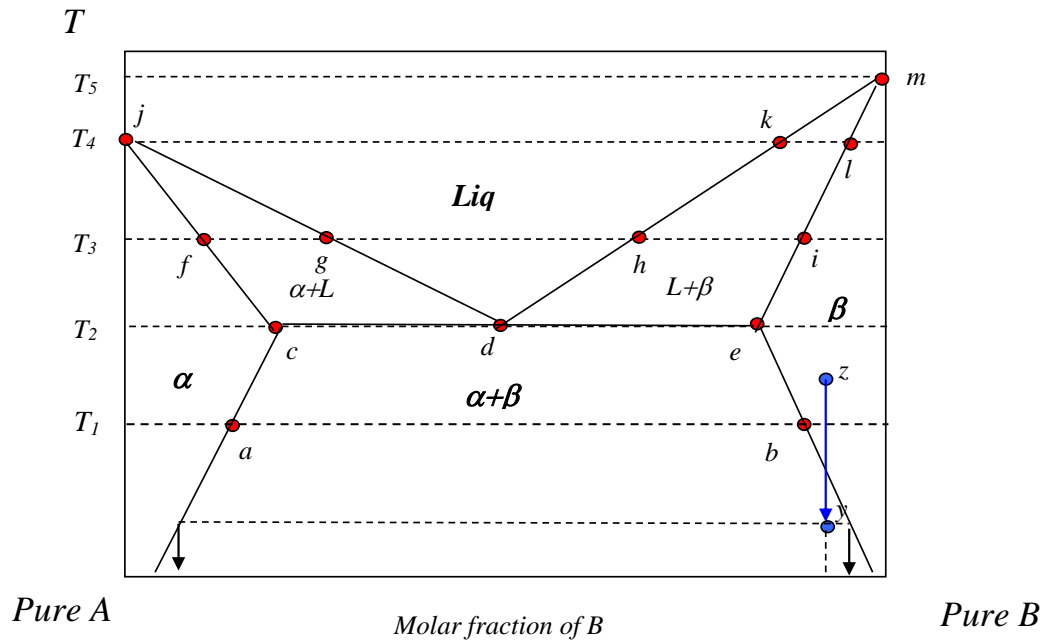
**Figure 10.3 Schematic phase diagram of a eutectic A-B system**

As illustrated in Fig. 10.3, plots of Gibbs energy vs. composition similar to that shown in Fig. 10.2 constructed at various temperatures can be used to construct the standard phase diagram, of which Figure 10.3 is an example.

Temperature T_1
Points x_1 and x_2 in Fig. 10.2 translate to a horizontal line in Fig. 10.3 extending between the two single-phase domains and indicating a composition region where at equilibrium a mixture of two phases is observed. The two-phase domain extends from *a* to *b*.

Temperature T_2
As the temperature increases above T_1, the Gibbs energy of the liquid decreases relative to the alpha and beta phases. At T_2 the three curves on the *g* vs. composition plot exhibit a single common tangent (upper left hand diagram in Fig. 10.4) at compositions *c, d* and *e* in Figs 10.3 and 10.4.
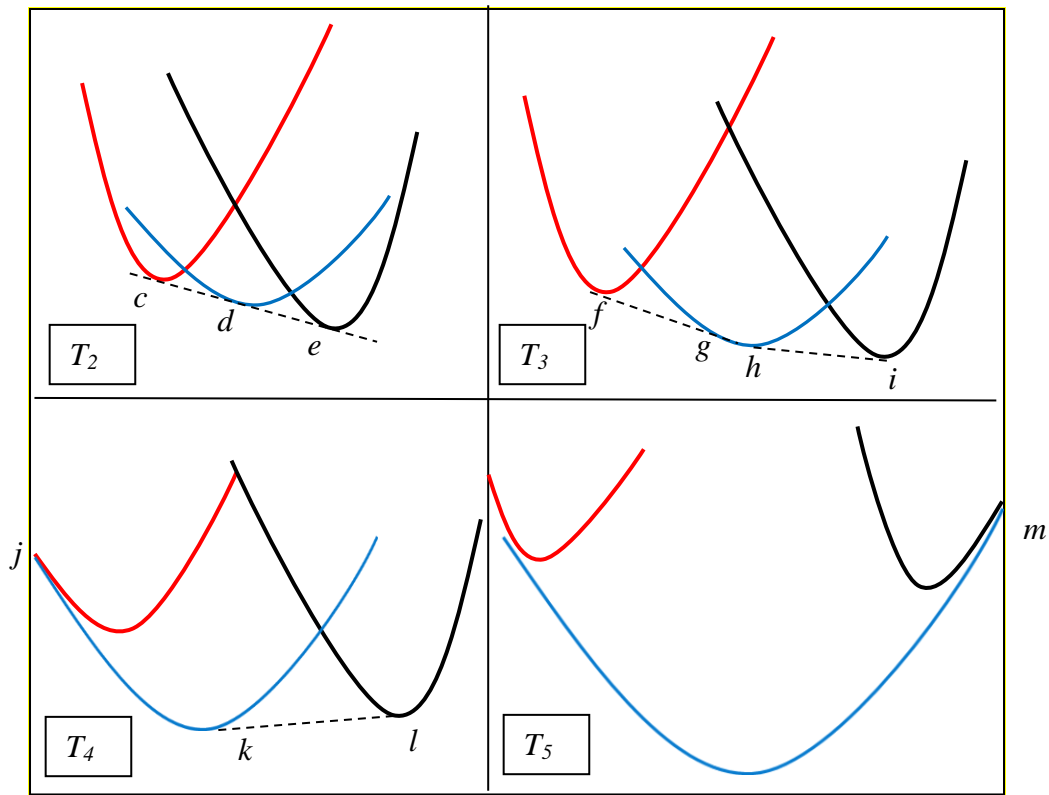
Fig. 10.4 Schematic Gibbs energy curves versus composition for the corresponding temperatures shown in Figure 10.3. The red curve is alpha, blue is liquid and black is beta.

At this temperature the three phases are in equilibrium at the compositions determined by the common tangent, which means by Eq (10.8) that at this temperature the atoms in the three phases at those compositions have the same chemical potential.

The lowest temperature and composition (point d) at which the liquid is stable is called the *eutectic* point. The eutectic transformation reaction may be written as

$$Liquid \xrightleftharpoons[\text{heating}]{\text{cooling}} \alpha + \beta \tag{10.9}$$

Note that the compositions of α and β just after the eutectic transformation (10.9) are c and e respectively, thus the liquid decomposes into two solids enriched in A and B.

Temperature T_3
As the temperature increases further, the Gibbs energy curve for the liquid falls below the common tangent of α and β so that there are now two common tangents, *f-g* (between α and liquid) and *h –i* (between liquid and β). In Fig. 10.3, two 2-phase regions (*f-g and h-i*) plus three single-phase domains (*0-f, g-h and i-1*) appear. In addition to the single-phase α and β regions at the edges (below f and above i, respectively), there is now a

liquid phase between points *g and h*. In between these phases there are two regions of two-phase equilibria, α + L and β + L (*f-g and h-i*).

Temperature T_4
Above temperature T_4, the Gibbs energy curve of the liquid becomes lower than that of the α phase throughout the *entire* compositional range and the *f-g* two-phase zone disappears from the phase diagram. This temperature then corresponds to the melting temperature of the alpha phase containing 100% A (point *j* in the two figures). The Liq+β two-phase zone persists, but is smaller. There is also a single-phase β region.

Temperature T_5
At this temperature the last remaining solid (100% B *β* phase) melts, so that this the lowest temperature at which there is only a single liquid phase. This temperature is the melting point of single-phase B in the β crystal structure (point *m* in Figs. 10.3 and 10.4).

By performing careful measurements of phase equilibria at a series of temperatures it is possible to construct a phase diagram such as shown by the lines in Fig. 10.4.

Order of Phase transformations
Finally, phase transformations can be classified by their *order*. A phase transformation is *first order* if during the phase transformation the change in Gibbs energy is zero but its *first derivative* is discontinuous at the transformation temperature:

$$\Delta \left(\frac{\partial g}{\partial T} \right)_{T_t, P} \neq 0 \qquad (10.10)$$

In such a transformation energy needs tp be supplied or removed. For example, the phase transformation illustrated in Figure 10.1 is first-order because as freezing/ melting occurs the Gibbs energy of the liquid or solid is continuous across the transformation (the curves match), but the first derivative of the Gibbs energy is *not continuous* (in the illustration, the first derivative of the liquid is higher than that of Sol_1 at the transformation temperature). This implies that first-order phase transitions have a *latent heat* of transformation, i.e. energy either needs to be supplied or is released at constant temperature for one phase to transform into another. Thus the phases coexist once the transformation is under way. For example when a bucket of ice melts into water, both ice and water coexist in the bucket until enough heat is supplied that all of the ice transforms to water.

For a *second-order* phase transformation the discontinuity occurs in the *second* derivative of the Gibbs energy with temperature. As a result, in a second-order phase transition, one phase changes into the other continuously, and the phases do not coexist during the transformation.

10.2.3. Examples of Important phase diagrams
In analyzing the materials for the core of a nuclear reactor, phase diagrams are particularly useful, notably those dealing with the alloys used for cladding and structural

materials and those related to the ceramic fuel material. Fig. 10.5 (a-i) shows calculated binary phase diagrams for the main alloying elements used in zirconium alloys for nuclear fuel cladding, Fe-C (relevant for steels) and U-O (the component of fuel).[3]

The region of greater interest in the Zr-M phase diagrams for our purposes lie in the Zr-rich part of the diagram, as the concentrations of alloying elements are generally low. The exception are the H and O phase diagrams in which Zr oxides and hydrides are depicted. The formation of zirconium hydrides and oxides shows up during in reactor operation.

The phase diagrams in Fig.10.5 show various features which illustrate different phase equilibria. The phase diagram of Zr-Sn (Fig. 10.5a) shows a large difference in melting temperature between the two constituents, so as the Sn content increases so does the stable liquid phase domain. Various line compounds (exact stoichiometry) appear such as Zr_4Sn and Zr_5Sn_3, but which are not observed in Zircaloy or ZIRLO, likely because of the slow kinetics of their formation. The Zr-Nb phase diagram (Fig. 10.5b) shows complete solid solubility in the beta phase at temperatures from about 1000 C to 1500 C. This means that bcc Zr transforms smoothly into bcc Nb as the Nb content increases without any phase separation. The beta phase shows also a region of spinodal decomposition (see section 10.4.4), and, more relevant to nuclear applications, the alpha Zr phase can take up about 0,4% Nb in solid solution. The Zr-O phase diagram (Fig. 10.5c) shows an equilibrium between Zr(O) solid solution and ZrO_2. Such an equilibrium is partially observed during waterside corrosion of zirconium alloys, since an oxygen rich region is normally observed ahead of the advancing ZrO_2 oxide layer. Because the oxide layer is constantly advancing   and consume the oxygen rich layer as it advances, it can only be said to be in a dynamic steady state. The Zr-H phase diagram (Fig. 10.5d) predicts the presence of zirconium hydrides as soon as the solid solution limit is exceeded, which is in fact seen in reactor, but because of kinetic reasons not necessarily in the most favorable region.

The Zr-Cr (Fig. 10.5e), Zr-Ni (Fig. 10.5f), and Zr-Fe (Fig. 10.5g) phase diagrams show very low solid solubility for all these elements in alpha Zr. Thus, as discussed in Chapter 17, they are mostly found in intermetallic precipitates. Because the transformation temperature for Zr_2Ni and $ZrCr_2$ is lower than that for Fe containing compounds, iron tends to appear as a substitutional solute in the Ni and Cr sublattices of these compounds. This is a simple example in which the presence of a third element affects the behavior of a binary system illustrating that ternary phase equilibria differ from binary equilibria.

The Fe-C phase diagram (Fig.10.5h) provides the basis for the development of the various steels used in the industry. It shows the alpha iron phase (bcc Fe), also called ferrite, at low temperature, and gamma Fe (fcc Fe) also called austenite, at higher temperature (for clarity, beta Fe concerns a magnetic transformation in the alpha range). Stainless steel consists of Fe alloyed with Ni and Cr which causes the austenite to be stable at low temperature. The resistance of austenitic steel to corrosion is much higher

[3] The phase diagrams in Figure 10.5 were graciously prepared by G.Lindwall and Z.K.Liu, and were calculated using Thermocalc (need reference)

than that of ferrite, as can be easily discerned in one's kitchen, by examining the behavior of carbon steel knives which show rust in contact with water and stainless steel flatware which does not. The reactor pressure vessel is made of ferritic steel while the reactor internals are of stainless steel. More discussion on this phase diagram is presented in Section 10.5.

Finally the U-O phase diagram illustrates the various phases of metallic uranium, including the low temperature face centered orthorhombic phase (see Chapter 3) and shows the UO_2 phase as having a small range of stability in the sub stoichiometric range, allowing to use UO_{2-x} as the oxide for fuel (Chapter 16).
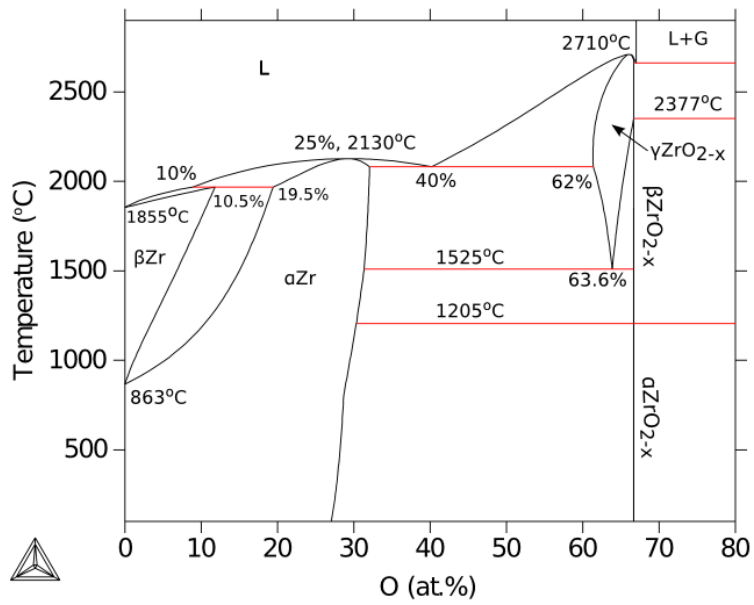
Fig. 10.5: Binary phase diagrams of importance to the nuclear industry: (a) Zr-Sn, (b) Zr-Nb, (c) Zr-O, (d) Zr-H, (e) Zr-Cr, (f) Zr-Ni, (g) Zr-Fe, (h) Fe-C, (i) U-O
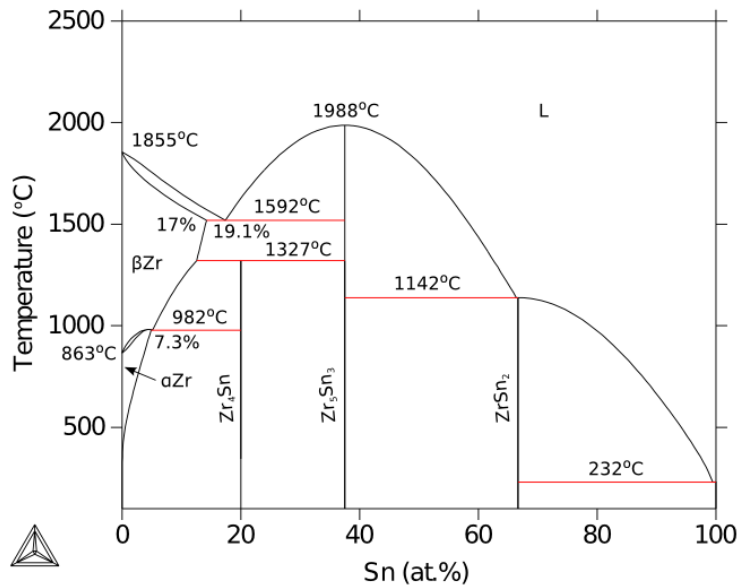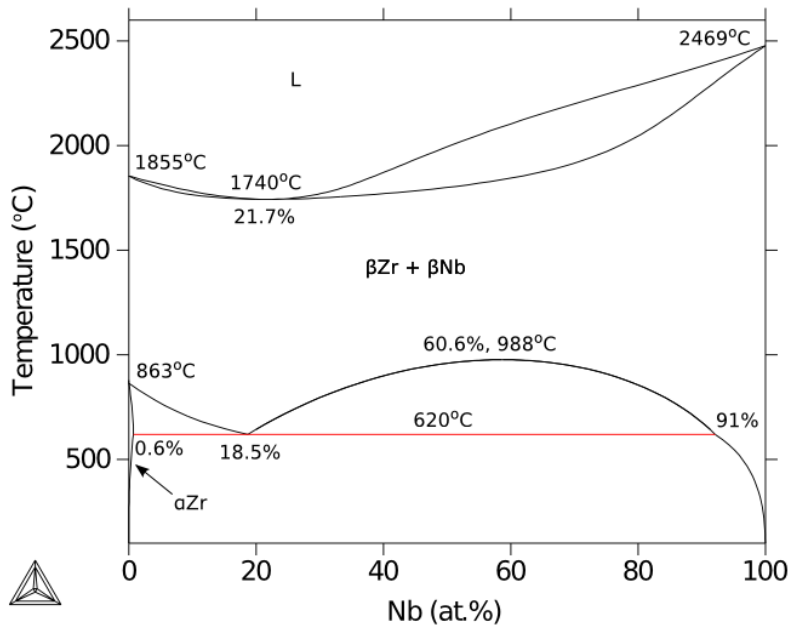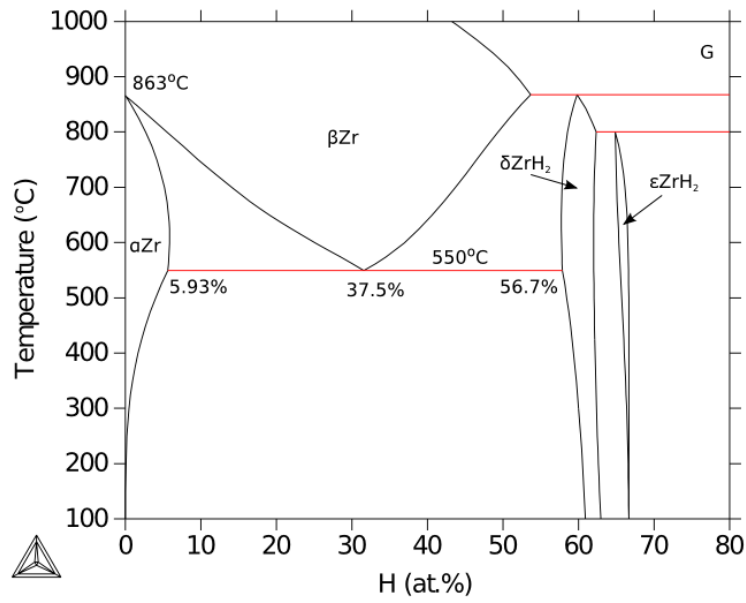
(b)

(c)

(d)
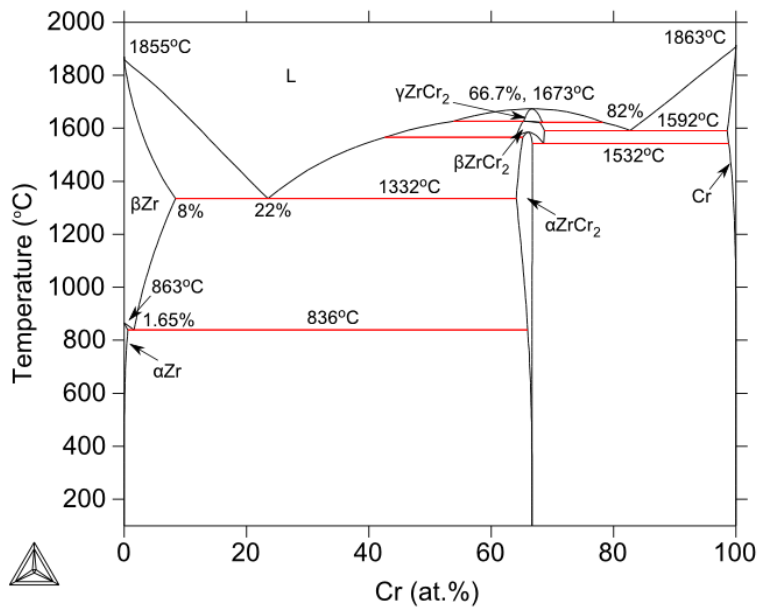
(e)

(f)

(g)

(h)

(i)

The Zr-M binary phase diagrams determine much of the microstructure of the fuel cladding, as discussed in Chapter 17. For example, the Zr-Cr phase diagram predicts that at a temperature of 300 °C and Cr content of a few %, the stable phases are α-Zr and ZrCr₂, which are in fact observed in Zircaloy, but with Fe substituting in the Cr

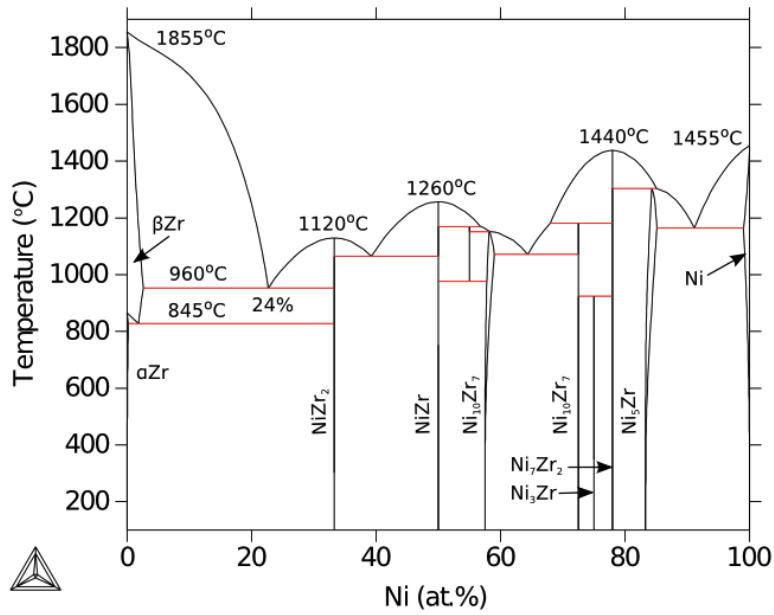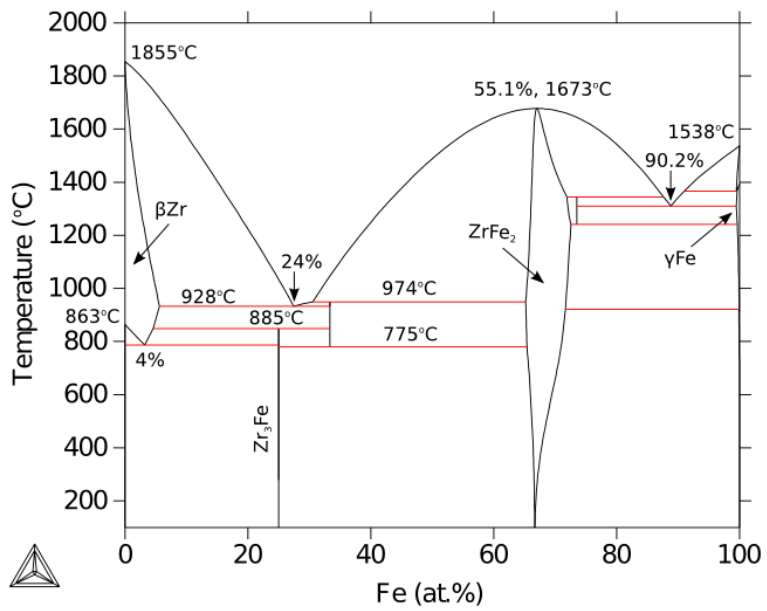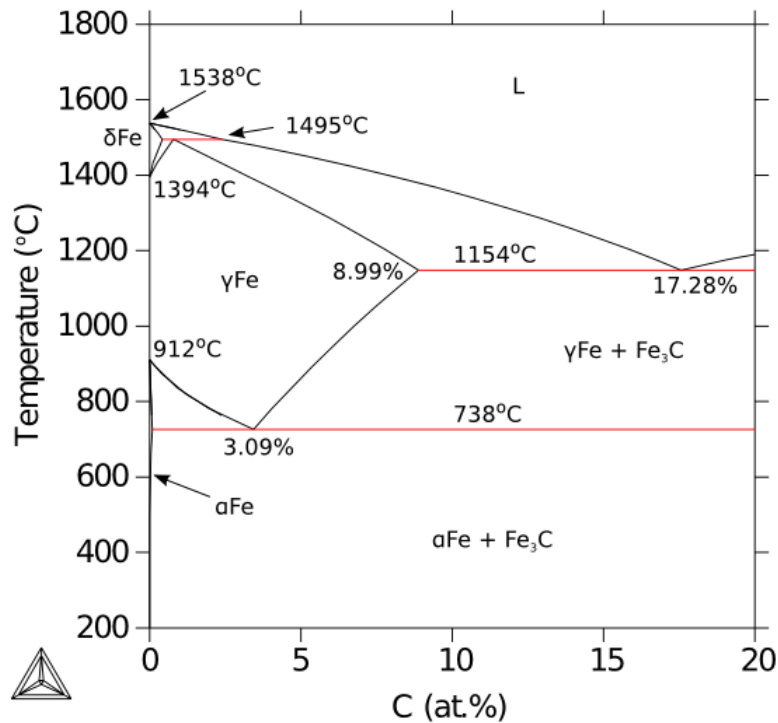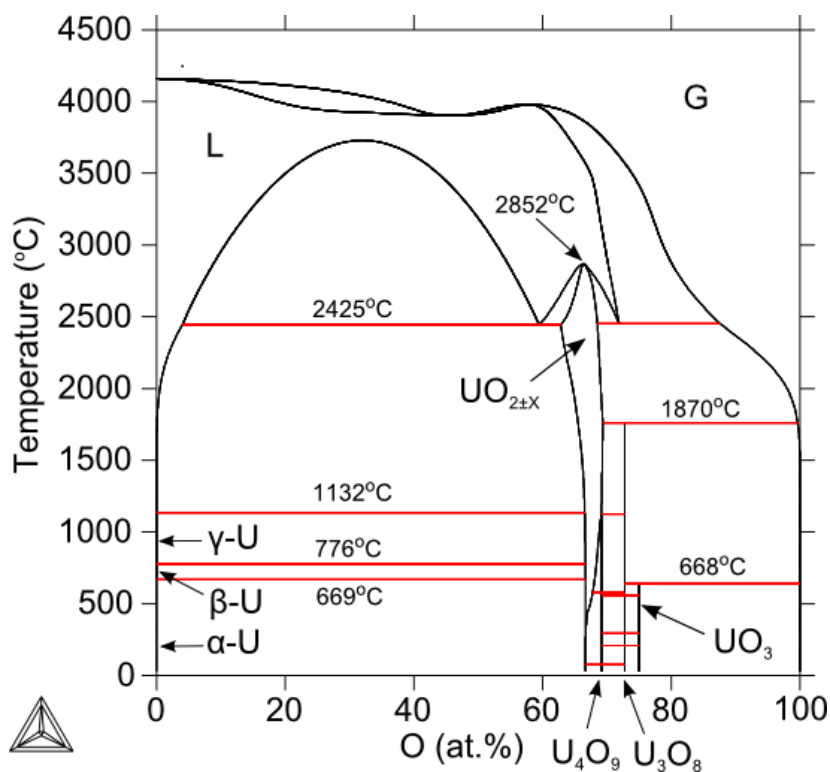sublattice, Zr(Cr,Fe)$_2$. The Zr-O phase diagram shows that only one oxide of zirconium (ZrO$_2$) is stable at temperatures of interest, but many sub-oxide metastable phases are often observed during cladding waterside corrosion. The Fe-C phase diagram is the basis for understanding the composition of steels. These alloys, however, contain more than one metal, so ternary and higher-order phase diagrams are needed to describe phase equilibria. These are, however, beyond the scope of this book.

10.3. Nucleation of a Second Phase

The first part of this chapter dealt with the driving forces for phase transformation, which govern the *direction* of a phase transformation. Once this is established it is necessary to address how the transformation takes place and the rate of the process needs to be calculated.

When no change in composition is involved, the transformation occurs in a *displacive* manner, in which the atoms move a small distance (within the unit cell) in coordinated fashion to create a new phase. One example of this is the phase transformations in ZrO$_2$ from cubic to tetragonal to monoclinic (Fig. 3.14). It is also possible to observe interface reaction controlled transformations, such as the $\beta \rightarrow \alpha$ transformation in Zr . Also recrystallization can be seen as this type of transformation since its kinetics are similar even though there is no change in crystal structure.

More commonly phase transformations involve compositional changes and large-scale transfer of matter; these are called *replacive* transformations as one type of atom needs to be replaced by another by long-range atomic transport.

The first step in a replacive transformation is the creation of a nucleus (*nucleation*) of a new phase (α) from an unstable matrix phase (β). In *homogeneous* nucleation, the new phase appears without the aid of inhomogeneities or defects in the matrix. In *heterogeneous* nucleation, defects such as grain boundaries, dislocations, or free surfaces aid the nucleation of the new phase.

10.3.1. Homogeneous nucleation

In replacive phase transformations, the creation of a new phase entails an energy cost associated with the formation of an interface between the nucleus of the new phase and the matrix in which it is embedded. The required energy has to be balanced by reduction in Gibbs energy associated with the formation of the new (more stable) phase. From this idea follows the theory of *homogeneous nucleation*.

Consider a β phase that has been cooled below the equilibrium temperature for the α and β phases (e.g., below T$_m$ in Fig. 10.1). Consider the nucleation of a spherical alpha phase particle from the beta matrix. The question of interest is: what is the minimum cluster

size that yields a stable α nucleus from a β-phase matrix? In this case, n_α moles of α are formed from the original β phase as determined by:

$$n_\alpha = \tfrac{4}{3}\pi\, r_\alpha^3 \rho_\alpha \qquad (10.11)$$

where ρ_α is the molar density of α. and r_α is the radius of the nucleus.

Let $\Delta g_{\alpha\beta} = g_\beta - g_\alpha$ be the difference in Gibbs energy per mole of β and α. This is a positive quantity, since the β phase is subcooled. The change in Gibbs energy upon formation of a single spherical nucleus of α phase is:

$$\Delta g_{hom} = \Delta g_{vol} + \Delta g_{surf} + \Delta g_{strain} \qquad (10.12)$$

where Δg_{vol} is the Gibbs energy change upon the transformation for the volume considered, Δg_{surf} is the interfacial energy that needs to be supplied to create a new phase and Δg_{strain} is the strain energy associated with a density change of the second phase with respect to the parent. This last term is often important and may determine the rate of nucleation, but it is not easily evaluated. If it is for the moment ignored, the Gibbs energy of nucleation is

$$\Delta g_{hom} \approx \Delta g_{vol} + \Delta g_{surf} = -n_\alpha \Delta g_{\alpha\beta} + \gamma_{\alpha\beta}(4\pi r_\alpha^2) \qquad (10.13)$$

where $\gamma_{\alpha\beta}$ is the interfacial energy of the α- β surface. Eliminating n_α between Eqs (10.11) and (10.12) yields:

$$\Delta g_{hom} = -\tfrac{4}{3}\pi\, r_\alpha^3 \rho_\alpha \Delta g_{\alpha\beta} + 4\pi r_\alpha^2 \gamma_{\alpha\beta} \qquad (10.14)$$

Equation (10.14) states that as a new particle is nucleated the Gibbs energy initially increases as the surface energy term dominates. As the radius increases further, the volume term eventually overtakes the surface term and the energy becomes negative, which means that it would be favorable for precipitation to occur.

Fig. 10.6 shows a plot of equation (10.14). The solid red curve is the surface energy term, while the solid blue curve is the volumetric decrease in Gibbs energy after the transformation and the black solid curve the sum of the two. When the derivative of the total Gibbs energy shown in the black curve becomes zero, any further increases will cause a decrease in Gibbs energy and therefore the growth of the particle can occur unimpeded. The point where the derivative is zero is called the critical radius for homogeneous nucleation of alpha phase, r_{crit}^α.
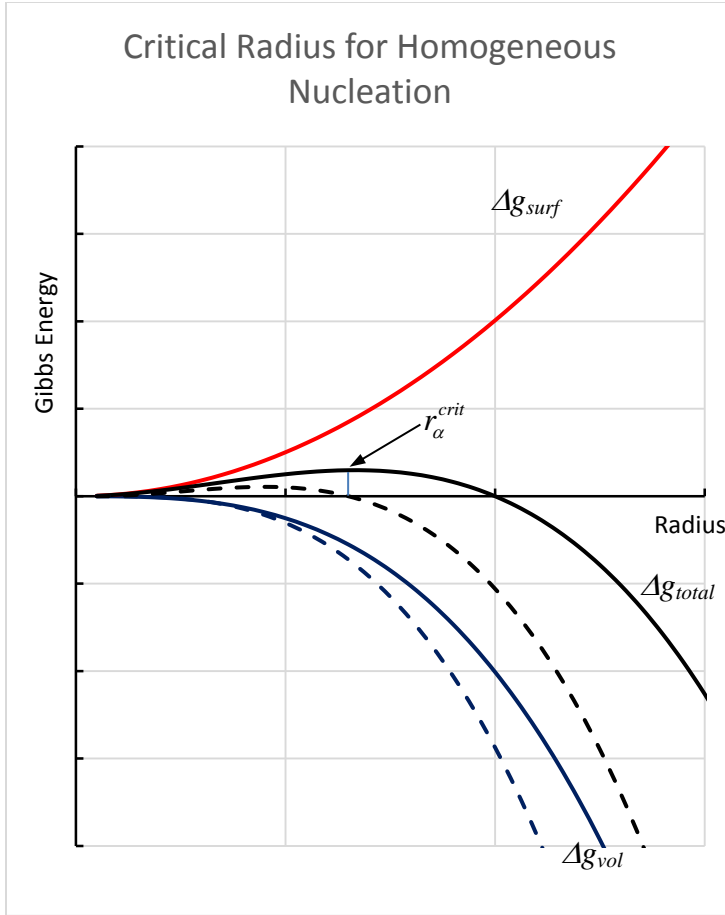
Fig. 10.6 Schematic plot of the Gibbs energies upon the formation of a spherical nucleus from solid solution. Dashed lines indicate the effect of greater undercooling.

This can be done formally by noting that

$$\frac{\Delta g_{hom}}{4\pi r'^2 \gamma_{\alpha\beta}} = -\left(\frac{r_\alpha}{r'}\right)^3 + \left(\frac{r_\alpha}{r'}\right)^2 \tag{10.15}$$

where:

$$r' = \frac{3\gamma_{\alpha\beta}}{\rho_\alpha \Delta g_{\beta-\alpha}} \tag{10.16}$$

Δg_{hom} in Equation (10.15) is positive for small values of r_α and becomes negative as r_α increases. When further increases in r_α cause a *decrease* in Gibbs energy the nucleus of the α phase becomes stable. Setting the derivative of Eq (10.15) to zero, which gives:

$$\frac{r_\alpha^{crit}}{r'} = \frac{2}{3} \quad or \quad r_\alpha^{crit} = \frac{2\gamma_{\alpha\beta}}{\Delta g_{\alpha\beta}} \tag{10.17}$$

If nucleation produces an α sphere phase with a radius $r_\alpha < r_\alpha^{crit}$, the nucleus dissolves back into the β phase. If $r_\alpha > r_\alpha^{crit}$ the nucleus is stable and continued attachment of atoms from the β phase (growth) further lowers the Gibbs energy. One could question how the critical radius is ever formed, since there will always be a radius below which growth is unfavorable. The thought is that random thermal fluctuations are constantly creating nuclei and when one of these randomly occurs above the critical size, its growth is thermodynamically favored.

Note that the nucleation rate (number of particles/second per unit volume) is given by

$$\frac{dN_\alpha}{dt} \propto \exp\left[\frac{-\Delta g_{crit}}{k_B T}\right] \qquad (10.18)$$

where Δg_{crit} is proportional to the critical radius. As Δg_{crit} decreases the nucleation rate increases. A high nucleation rate will then occur when precipitates are small (by forming coherent precipitates or by heterogeneous nucleation, see following section) or by large negative $\Delta g_{\alpha\beta}$.

As shown in Fig.10.1 for the liquid (β) - solid (α) transformation, the Gibbs energy difference between the β and α phases, $\Delta g_{\alpha\beta}$, is zero at T_M and increases with undercooling. From equation (10.17) it can be seen that the critical radius is inversely proportional to the free energy difference. The effect of increased undercooling is shown in the dashed plots of Fig.10.6 in which the Gibbs energy change was increased by 2/3 relative to the initial calculation. It is clear that the critical radius decreases in proportion.

Determination of a numerical value of the critical radius requires knowledge of the interfacial energy $\gamma_{\alpha\beta}$ and the Gibbs energy difference between the β and α phases for the extent of subcooling. If the curves in Figure 10.1 can be approximated as straight lines it can be shown that

$$\Delta g_{\alpha\beta} = \frac{L_M \Delta T}{T_M} \qquad (10.19)$$

where L_M is the latent heat of melting, ΔT is the undercooling and T_M the melting temperature. Substituting Eq. (10.19) into Eq. (10.17) the critical radius for solidification is:

$$r_\alpha^{crit} = \frac{2\gamma_{\alpha\beta} T_M}{L_M} \frac{1}{\Delta T} \qquad (10.20)$$

For copper $T_M =1365$ K, $\gamma_{ab} = 0.18$ J/m^2 and $L_M= 1.9 \times 10^9$ J/m^3, the critical radius as a function of the undercooling given by Eq. (10.20) is plotted in Figure 10.7 .
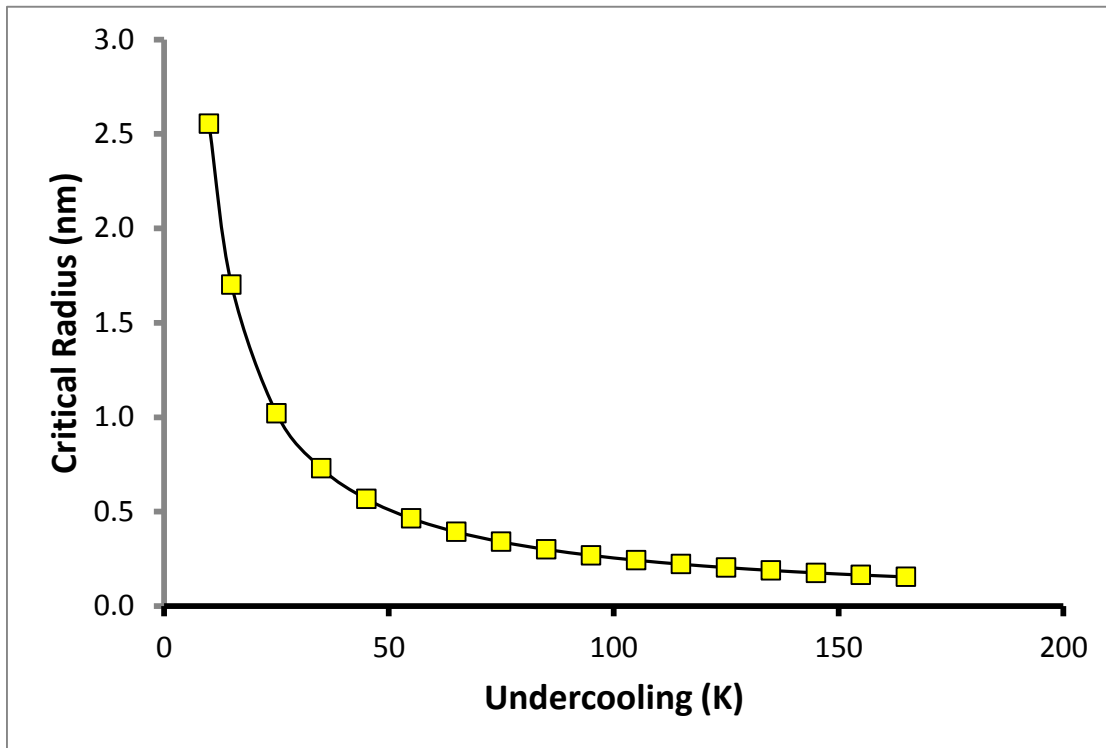

Fig. 10.7 Critical radius of nucleus for precipitation of solid Cu from the liquid at 1365 K

The plot in Fig.10.6 shows that for $\Delta T = 10^{\circ}$C the critical radius for solidification is 2.5 nm, which decreases to less than 0.5 nm at 50° C undercooling.

10.3.2. Heterogeneous Nucleation

Because real crystals have defects and impurities, homogeneous nucleation hardly ever occurs. Imperfections dramatically reduce the interfacial energy that must be supplied, thereby providing an easier path for phase transformation. For example, when boiling water in a pot, bubble nucleation occurs at the bottom surface (in fact if one looks closely at scratches in the bottom of the pan this is where bubbles form first). By analogy, when casting metals, the mold surface can provide nucleation sites for the solid to form from the liquid phase. This process is called heterogeneous nucleation.

Decreasing the surface energy will also reduce the critical radius and facilitate precipitation. This is shown in Fig. 10.8, in which the area needed for surface formation was reduced by one half.
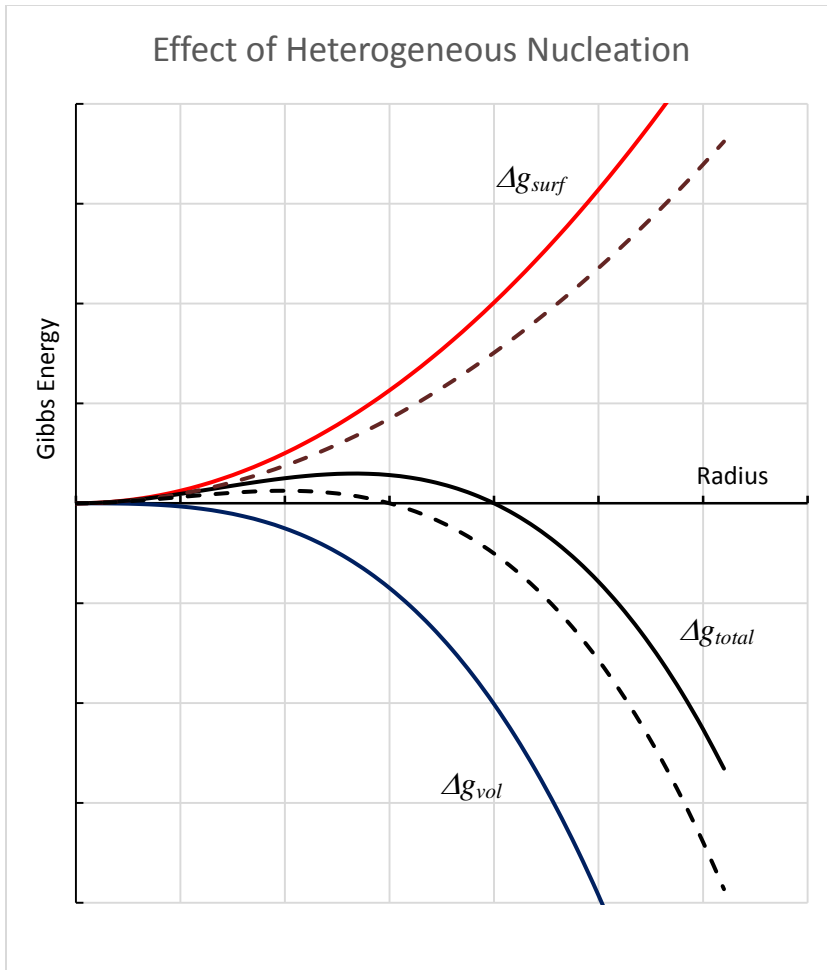
Fig.10.8 Effect of lower surface energy (dashed line) on the Total Gibbs energy

The effect of heterogeneous nucleation on the phase transformation can be modeled by a spherical cap of the new phase (α) forming on a surface (S), as shown in Fig. 10.9. The upper portion represents the single-phase β phase and $\gamma_{S\alpha}$, $\gamma_{S\beta}$ and $\gamma_{\alpha\beta}$ denote interfacial energies at the three interfaces, surface-α, surface-β and α-β.
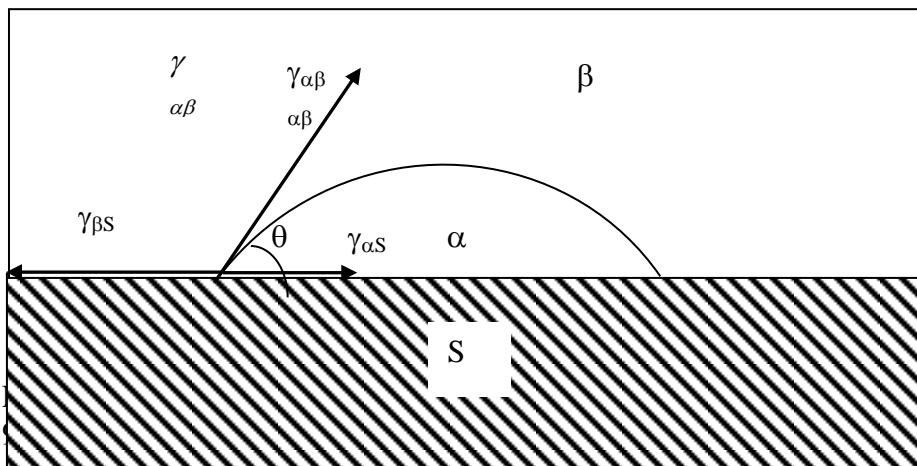
Figure 10.9: Heterogeneous nucleation at a surface (after [2], as cited by [3].)

The Gibbs energy change associated with forming a nucleus of the α phase from the β matrix on the surface S is given by:

$$\Delta g_{het} = -\Delta g_{\alpha\beta} n_\alpha + \gamma_{\alpha\beta} A_{\alpha\beta} + \gamma_{\alpha S} A_{\alpha S} - \gamma_{\beta S} A_{\alpha S} \tag{10.21}$$

where the A_{ij} are the areas of the i-j interfaces.. The first term corresponds to the decrease of the Gibbs energy (per mole) in transforming n_α from β to α; the second and third terms are the energies of the interfaces between the α and β phases and between α and the surface S. The last term is a reduction in the Gibbs energy resulting from the elimination of the β–S interface. Equilibrium of forces at the edge of the nucleus in Fig. 10.9 is:

$$\gamma_{\beta S} = \gamma_{\alpha S} + \gamma_{\alpha\beta} \cos\theta \tag{10.22}$$

Substituting equation (10.22) into (10.21) yields:

$$\Delta g_{het} = -\Delta g_{\alpha\beta} n_\alpha + \gamma_{\alpha\beta} A_{\alpha\beta} - (\gamma_{\alpha\beta} \cos\theta) A_S \tag{10.23}$$

From the geometry in Fig. 10.9, the number of moles of B in the spherical cap is

(i) $n_\alpha = \rho_\alpha \pi r^3 (2 + \cos\theta)(1 - \cos^2\theta)/3$,

   Where ρ_α is the molar density of α phase. When $\theta = \pi$, n_α reduces to half the value of Eq (10.10), (half a sphere).

(ii)   the area of the cap is $A_{\alpha\beta} = 2\pi r^2(1-\cos\theta)$

(iii)   the area of the wall surface-beta interface is $A_{\beta S} = \pi r_\alpha^2 \, sin^2\theta$ where r_α is the radius of the spherical cap of the α phase.

The result is:

$$\Delta g_{het} = \rho_\alpha \frac{\pi r^3 \Delta g_{\alpha\beta}(2+\cos\theta)(1-\cos^2\theta)}{3} + \gamma_{\alpha\beta}\pi r^2 \left[2(1-\cos\theta)+\sin^2\theta\cos\theta\right] \tag{10.24}$$

or: $\Delta g_{het} = \left[\rho_\alpha \dfrac{4\pi r^3 \Delta g_{\alpha\beta}}{3} + 4\pi r^2 \gamma_{\alpha\beta} \right] f(\theta) = \Delta g_{hom} f(\theta)$ 　(10.25)

with

$$f(\theta) = \frac{(2 - 3\cos\theta + \cos^3\theta)}{4}$$ 　(10.26)

Because f(θ) is between 0 and 1, *heterogeneous nucleation diminishes the Gibbs energy barrier compared to homogeneous nucleation*. That is, according to this model, $\Delta g_{het} < \Delta g_{hom}$.

As can be seen from Fig. 10.10 f(θ) → 1 when θ → π. That is, a sphere of α immersed in a β matrix without touching the surface S is equivalent to homogeneous nucleation. When θ →0, cos θ → 1 and f(θ) → 0, or the α phase "wets" the surface S. In this case only a very small amount of energy is needed for nucleation, related to the edges of the disk, which are neglected above and the α phase spontaneously replaces the β phase adjacent to surface S.

Differentiation of Eq (10.25) with respect to r_α (by Eq (10.22), θ is independent of r_α) and setting the result equal to zero gives the critical radius:

$$\left(r_\alpha^{crit} \right)_{het} = \left(r_\alpha^{crit} \right)_{hom} = \frac{2\gamma_{\alpha\beta}}{\Delta g_{\alpha\beta}}$$ 　(10.27)

That is, the radius of the spherical cap of α is the same as the radius of the entire sphere of α in homogeneous nucleation.
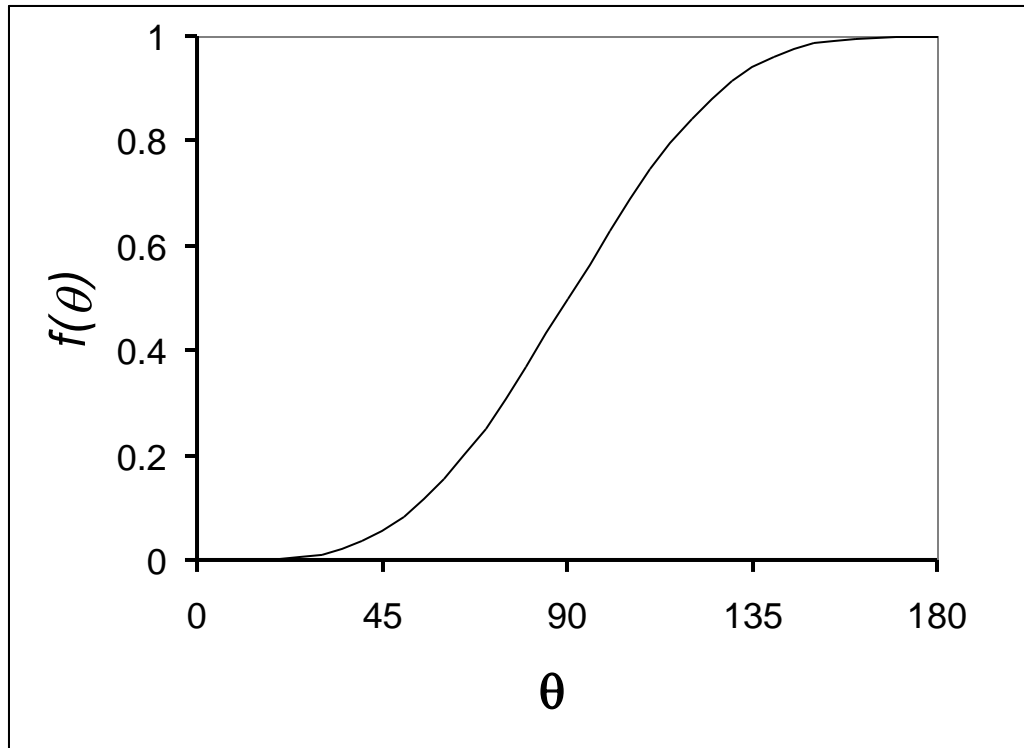
Fig. 10 10 The function f(θ) vs. θ

The Gibbs energy change for the formation of a critical radius is

$$\Delta g_{crit}^{het} = \frac{16\pi\gamma^3}{3(\Delta g_{vol})^2} f(\theta) \tag{10.28}$$

Other surfaces or defects can also serve as nucleation sites. In particular grain boundaries and especially triple points (Fig. 8.5) provide additional reduction of the Gibbs energy required for phase nucleation. Also, $\left(r_\alpha^{crit}\right)_{het}$ with the additional nucleation sites is lower than that given by Eq (10.20). The practical implication is that heterogeneous nucleation is easier than homogeneous nucleation because of the nucleation sites aid in the transformation. For example, salt water boils at a lower temperature than pure water because the salt acts as a nucleation site for formation of the steam phase[4]. Another example is the seeding of clouds by throwing solid particles from airplanes into rain clouds, which causes the water vapor to condense and produce rain.

10.4. Phase-Transformation Kinetics

---

[4] Note that this is a kinetic phenomenon; thermodynamically, a higher temperature is required to reach 1 atm vapor pressure in salt water than in pure water.

In the previous sections the reaction direction of a solid-solid phase transformation was discussed. The question can now be posed, as to *how fast* does a given transformation occur, that is the phase transformation kinetics. This is discussed in this section.

10.4.1 Homogeneous nucleation and growth in a single-component system

Consider a single-component, initially single β phase system in the absence of surfaces, crystal defects or impurities. When the temperature falls below the phase-transformation temperature, homogeneous nucleation occurs. Once formed, nuclei of the α phase continue to grow by absorbing atoms from the β matrix. It is of interest to know how fast the beta to alpha transformation occurs, that is how fast the alpha volume fraction increases.

The key aspect of the kinetics of phase-transformation by homogeneous nucleation and subsequent growth of the nuclei is the rate of increase of the fraction of a unit volume of initial β phase that has been converted to α phase. Figure 10.9 shows the two-phase mixture, but the following analysis does not account for attachment of the growing spheres.
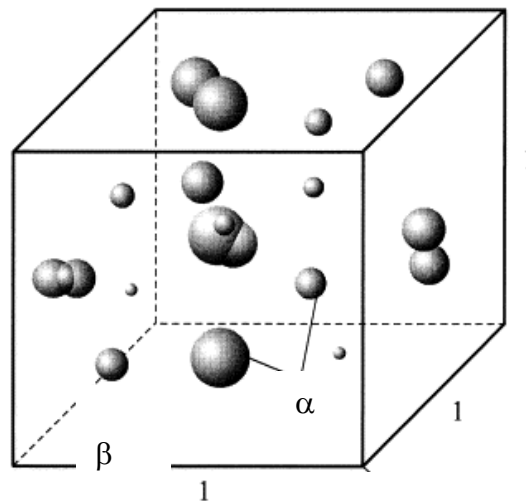
Fig. 10.11 Spheres of α phase in an initial unit volume of β phase

In this context, $V_\alpha(t)$ is the volume fraction of the α-phase spheres at time t since the start of nucleation. The two restrictions are:

1) The rate of α nucleation per unit volume of <u>remaining</u> β is constant at $\frac{dN}{dt}$. The volume fraction of β phase at time t' is *1-V_α(t')*, at which time the rate of nucleation of α is *[1-V_α(t')]* $\frac{dN}{dt}$.

2) Following nucleation, the growth rate *dr/dt* (i.e. the rate of increase of the radii of the α spheres) is constant at $\dot{r}_\alpha$ so at time t, the radius of a nucleus formed at time t' is $\dot{r}_\alpha \times$*(t-t')*

Consequently, the incremental volume of α at time t due to nucleation in the time period dt' is the product of the number of nuclei created in dt' and their volume at time t:

$$dV_\alpha = \tfrac{4\pi}{3}\left[\dot{r}_\alpha(t-t')\right]^3 \times \left[1-V_\alpha(t')\right]\dot{N}\,dt' \qquad (10.29)$$

integrating t' from 0 to t and V_α(t') from 0 to V_α(t) :

$$V_\alpha(t) = 1 - \exp\left(-\tfrac{\pi}{3}\dot{r}_\alpha^3 \dot{N} t^4\right) \qquad (10.30)$$

This is the *Johnson-Mehl-Avrami-Kolmorogov* equation. No explicit assumption has been made concerning the growth mechanism, except for the constancy of the nucleation rate and the growth rate of the α phase. Equation (10.30) predicts a transformation rate that is fast at the beginning but gradually slows down, showing a characteristic *S*-shapes in the curves in Fig. 10.12.

Both the growth rate $\dot{r}_\alpha$ and the nucleation rate $\dot{N}$ are strongly temperature-dependent. As the temperature decreases:

3) the nucleation rate increases as the undercooling increases since the thermodynamic driving force is greater, as shown by the double arrows in Fig. 10.1.

4) $\dfrac{dr_\alpha}{dt}$ decreases because of the slower atom diffusion rate resulting in a decreased rate of atom transfer from β to the α spheres at the interface.
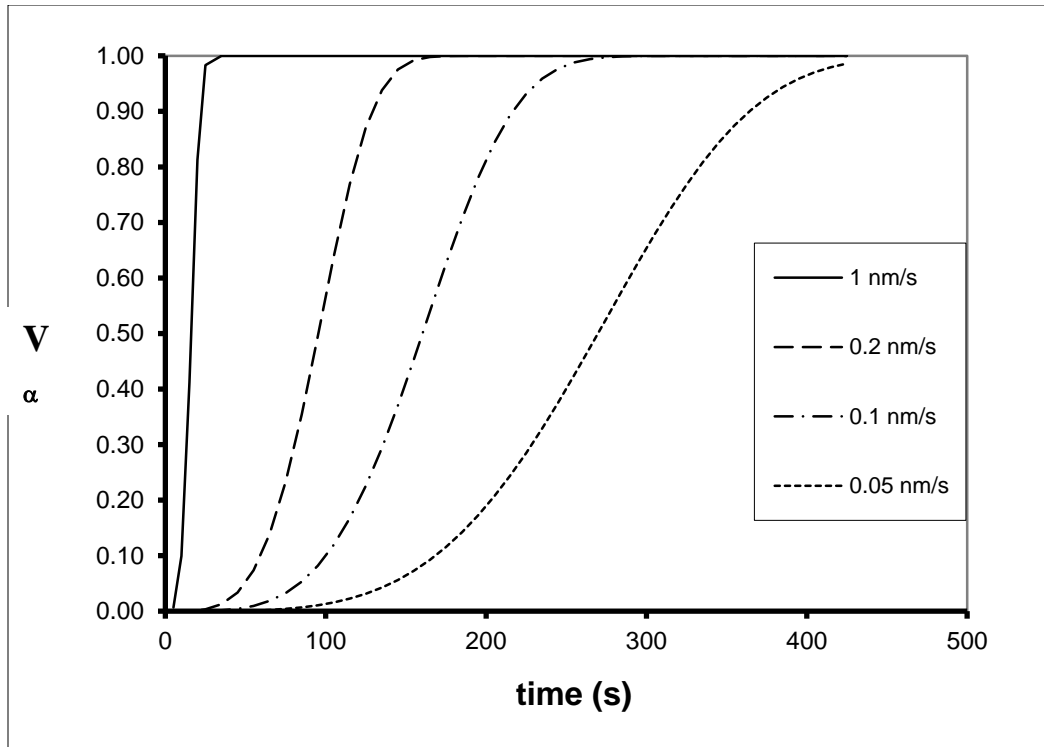
Figure 10 12: Fraction of phase transformed during homogeneous nucleation for various interfacial velocities $\dot{r}_\alpha$ in nm/s. The nucleation rate is 10^{18} nuclei/cm^3-s.

Other assumptions about the nucleation and growth rates lead to the more general formulation than Eq (10.30):

$$V_\alpha(t) = 1 - \exp\left(-k\,t^n\right) \qquad (10.31)$$

with n a constant depending on the nucleation and growth mechanism and *k* a factor that depends strongly on the temperature [4].

10.4.2 Interfacial reactions in two-component systems

Since the system contains two components, growth of the α phase depends on the sequential processes of atomic migration by diffusion of component B in the β phase:

$$B(\beta)_{bulk} \rightarrow B(\beta)_{int} \qquad (10.32)$$

followed by transfer of B atoms to the α phase at the α/β interface:

$$B(\beta)_{int} \rightarrow B(\alpha)_{int} \qquad (10.33)$$

The solute (B) concentration profile in the matrix assumes different shapes depending on which process is faster.

5) In the case of fast atomic diffusion compared to the reaction kinetics, Eq.(10.33), the flux of B is sustained without a significant solute-B gradient in the β matrix.

6) If the interfacial reaction is fast, a solute-depleted region appears in the matrix near the advancing interface. This diffusion limit is analyzed in the next section.

.

10.4.3 Diffusion-controlled growth in a binary solid state system

The question can now be posed as to what would the equivalent calculation of a phase transformation kinetics be in the case of a two-component system for a solid-solid transformation. That is when two different atoms are present, how does the growth of one phase from another occur? We consider here a simple one-dimensional case, as the process is quite complex.

Consider the phase diagram of a two-component, A and B system shown in Fig. 10.3a. A solid solution of the β phase, initially at point z with mole fraction of B given by x_β^y, is cooled rapidly to point y in the α+β two-phase region. Because single-phase β at point *y* is thermodynamically unstable, the second phase nucleates and grows. The new solid has both the structure and composition of the α phase, which is leaner in element B than the β phase .

$V_\alpha(t)$

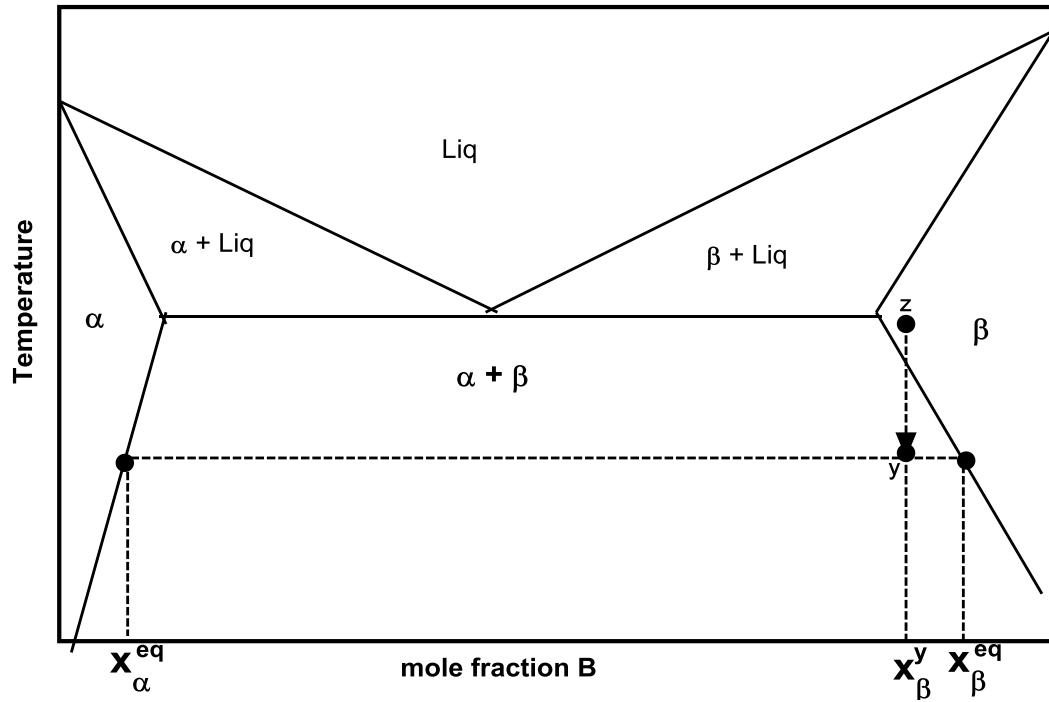**10.3a Binary phase diagram showing cooling from z to y and separation into immiscible phases α and β**

For simplicity, the β→α conversion is considered for the case of a planar interface of alpha growing into beta, rather than the most likely physical case of spherical particles. Initially, the nucleation stage produces a thin layer of the α phase which thereafter grows by diffusion of component B from the β phase. After some time, Fig. 10.13 shows an α phase of half- thickness L in a β matrix that occupies the remainder of the container of dimension Z. x_β^{eq} and x_α^{eq} are the equilibrium concentrations of component B in the β and α phases, respectively, that prevail at the interface between the two phases. There is a B-composition gradient in the β phase but none in α because it is formed at the equilibrium (phase-diagram) composition.
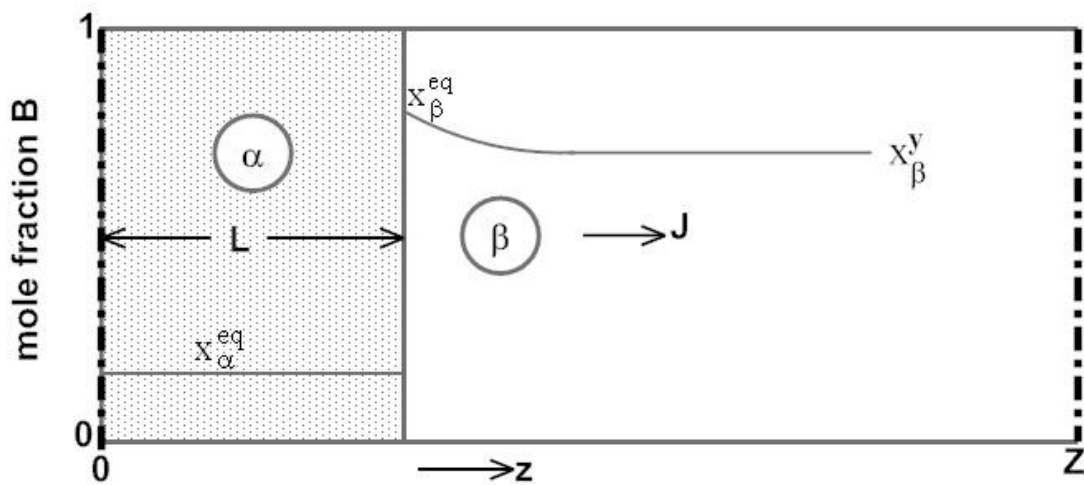
Fig. 10.11 Growth of an α particle into a β phase in a container of half-width Z

The physical case being considered is the precipitation reaction needed to effect the reaction

$$\beta(x_\beta^y) \rightarrow \beta(x_\beta^{eq}) + \alpha(x_\alpha^{eq}) \tag{10.34}$$

that is, the transformation from single phase beta at composition x_β^y to alpha + beta at the equilibrium compositions.

Because both alpha and beta phases are solids, their molar densities are considered to be approximately the same, and are designated by ρ. This approximation means that there is no volume change as β is converted to α at the interface.

The flux of component B (J in moles/cm^2-s) in the β phase is described by Fick's first law:

$$J = -\rho D_{AB} \frac{\partial x_\beta}{\partial z} \tag{10.35}$$

and Fick's second law is:

$$\frac{\partial x_\beta}{\partial t} = D_{AB} \frac{\partial^2 x_\beta}{\partial z^2} \tag{10.36}$$

In these equations, D_{AB} is the mutual diffusion coefficient of the A-B solid solution and t is the time since the original β phase was cooled to the temperature at point y.

Movement of the interface is controlled by a balance on component B:

$$\rho x_\alpha^{eq} \frac{dL}{dt} + J(L) = \rho x_\beta^{eq} \frac{dL}{dt} \tag{10.37}$$

$$\text{out} \qquad \text{in}$$

Because the α phase is growing, dL/dt is positive, so relative to the moving interface, the first term on the left is the convective flux of component B leaving the interface in the $-z$ direction. The flux J(L) is positive in the $+z$ direction (Fig. 10.11), so it represents *removal* of component B from the interface. The term on the right in Eq(10.37) is the input of B to the interface from the matrix, which is effectively moving to the left relative to the interface.

Rearranging Eq (10.37) and using Eq(10.35):

$$\frac{dL}{dt} = \frac{J(L)/\rho}{x_\beta^{eq} - x_\alpha^{eq}} = -\frac{D_{AB}}{x_\beta^{eq} - x_\alpha^{eq}} \left(\frac{\partial x_\beta}{\partial z} \right)_{z=L} \tag{10.38}$$

Equations (10.36) and (10.38) are to be solved simultaneously with the initial conditions:

$$x_\beta(z,0) = x_\beta^y \qquad L(0) = 0 \tag{10.39}$$

and the boundary conditions:

$$x_\beta(L,t) = x_\beta^{eq} \qquad \left(\frac{\partial x_\beta}{\partial z} \right)_{z=Z} = 0 \tag{10.40}$$

The equations are made dimensionless in the following.

independent variables:

$$\eta = \frac{z}{Z} \qquad \tau = \frac{D_{AB}t}{Z^2} \tag{10.41}$$

dependent variables:

$$\theta = \frac{x_\beta - x_\beta^y}{x_\beta^{eq} - x_\beta^y} \qquad\qquad W = \frac{L}{Z} \qquad\qquad (10.42)$$

With the above, Eqs (10.36) and (10.38) become:

$$\frac{\partial \theta}{\partial \tau} = \frac{\partial^2 \theta}{\partial \eta^2} \qquad\qquad (10.43)$$

$$\frac{dW}{d\tau} = -g\left(\frac{\partial \theta}{\partial \eta}\right)_{\eta=W} \qquad\qquad (10.44)$$

where:

$$g = \frac{x_\beta^{eq} - x_\beta^y}{x_\beta^{eq} - x_\alpha^{eq}} \qquad\qquad (10.45)$$

The initial conditions become:

$$\theta(\eta,0) \;=\; 0 \qquad\qquad W(0) \;=\; 0 \qquad\qquad (10.46)$$

and the boundary conditions:

$$\theta(W,t) \;=\; 1 \qquad\qquad \left(\frac{\partial \theta}{\partial \eta}\right)_{\eta=1} = 0 \qquad\qquad (10.47)$$

Before showing typical results, the equilibrium limit is determined. As time becomes very large, the α/β two-phase system attains equilibrium when the thickness of the α phase reaches L_∞. This limit is determined by conservation of component B: The quantity of B at the starting condition represented by point y in Fig. 10.3a is $Z x_\beta^y$ (the molar density ρ is omitted because it appears in all terms in this balance equation and so cancels out). In the final state, the concentrations of in both phases are the equilibrium values, so the quantity of component B is $L_\infty x_\alpha^{eq} + (Z - L_\infty) x_\beta^{eq}$. Equating the initial and final quantities of component B and solving for L_∞ yields:

$$\frac{L_\infty}{Z} = \frac{x_\beta^{eq} - x_\beta^y}{x_\beta^{eq} - x_\alpha^{eq}} = g \qquad\qquad (10.48)$$

Where g is given by Eq (10.45).

The dimensionless equations are solved using an explicit time-step, finite-difference scheme.

Figure 10.14 shows the B mole fraction profiles for four dimensionless times and for $\tau = \infty$. In the final equilibrium state, the α half-thickness occupies 36% of the container

volume and the β phase takes up the remaining 64%. Figure 10.15 shows the rate of approach of the α-phase half-thickness as a function of dimensionless time. The final equilibrium is attained at τ ~ 0.6.
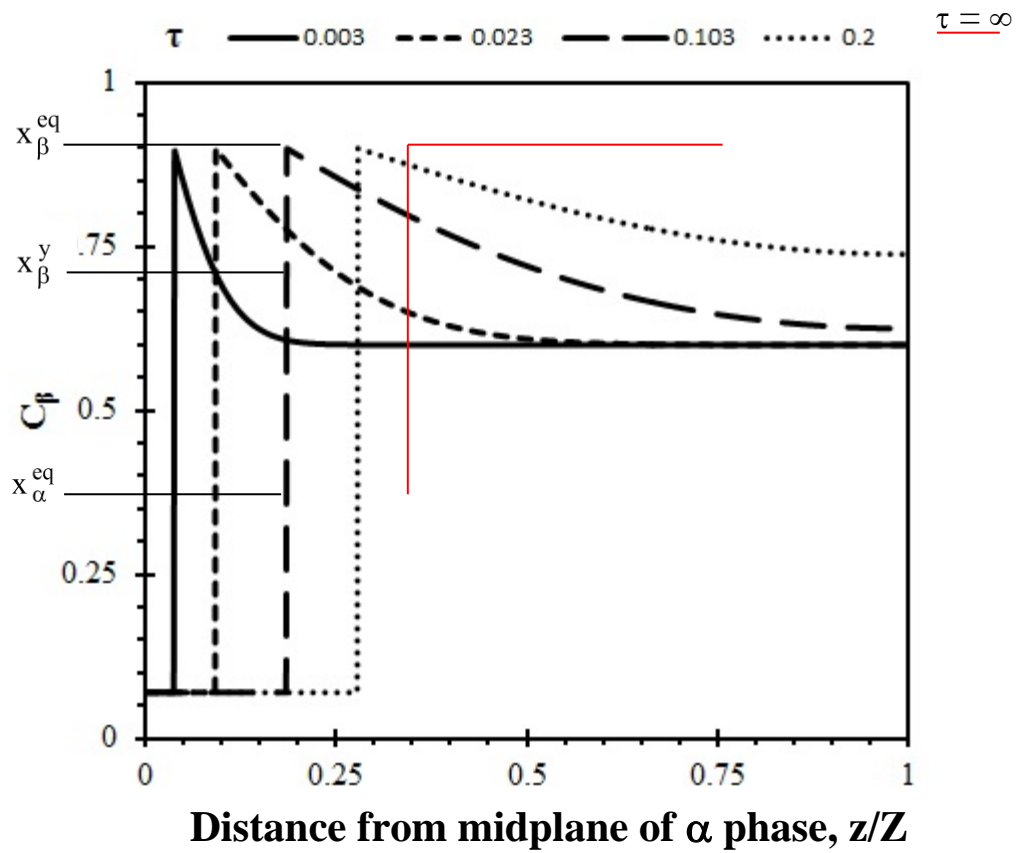
Fig. 10.14 Kinetics of phase separation according to equation (10.34)
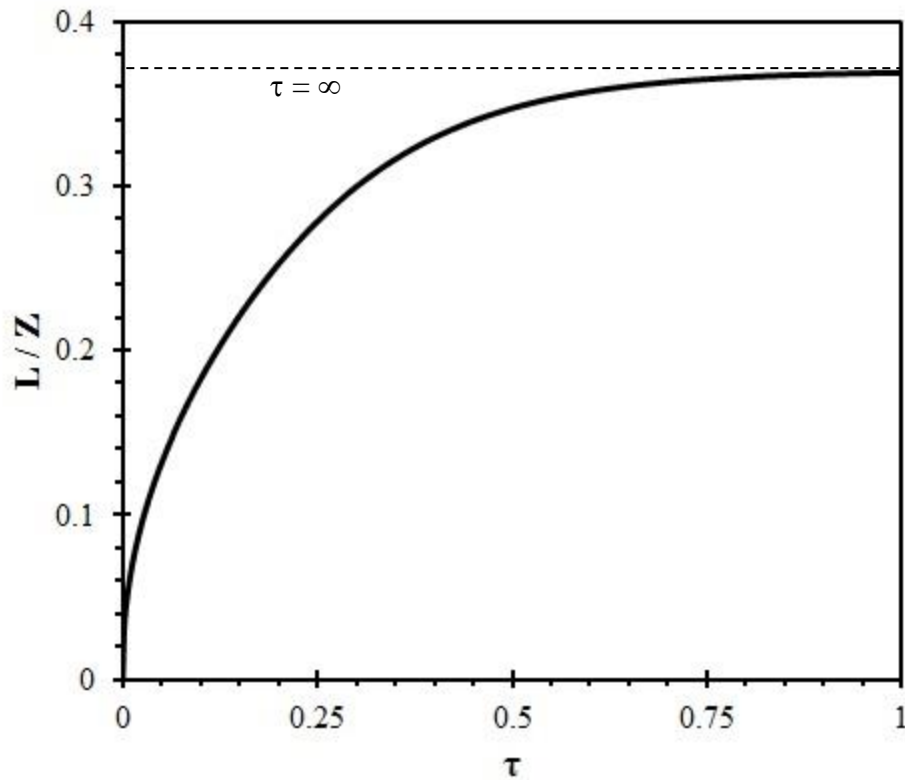
Fig. 10.15: Length of alpha phase as a function of dimensionless time

NEED Description of Figure 10.15

10.4.4. Transformation-Time-Temperature (TTT) diagrams

A convenient way to illustrate the fraction transformed in terms of the time elapsed at a certain temperature is given by *transformation-time-temperature* (TTT) diagrams. These are obtained from successive isothermal curves of the fraction transformed after time t.
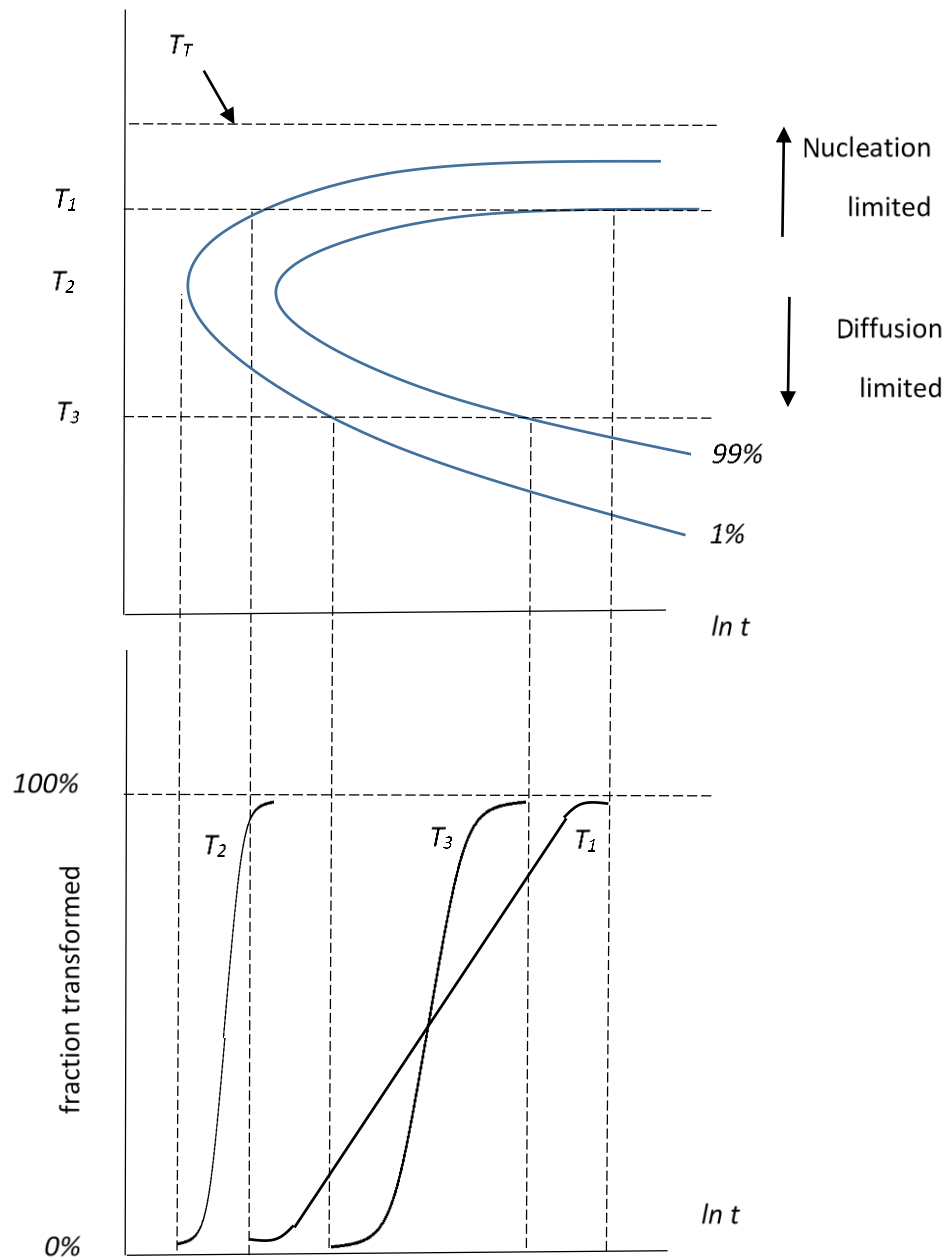
Figure 10.16: Schematic temperature time transformation diagrams for three different temperatures (adapted from [4])

The transformation process is depicted in Fig.10.16, in which the curves showing the degree of 1% transformation and 99% of the transformation effected are shown as a function of temperature. At the transformation temperature T_T the driving force for the transformation is zero. As the temperature decreases further the driving force for the transformation increases, which decreases the time to transformation (temperature T_1). Further increases cause the time to transformation to be reduced even more (temperature T_2). Below T_2 the atomic mobility decreases, at which point the nuclei that are present

cannot grow fast, and thus the time to transformation again increases (temperature T_3). If the TTT diagram is known, a cooling rate can be approximately designed to achieve a certain degree of transformation. The kinetics of fraction transformed are shown in the lower part of Figure 10.16 and should follow the S-shaped curve described in Equation (10.30).

Spinodal decomposition
In the phase transformations described above, there is a nucleation barrier, and phase formation occurs by a nucleation and growth process. This mechanism is valid when the second derivative of the Gibbs energy with respect to composition is positive. When the second derivative of the Gibbs energy is negative, phase formation occurs by *spinodal decomposition*

$$\frac{d^2g}{dx^2} < 0 \qquad (10.49)$$

One such situation occurs when the Gibbs energy curve for a given phase (called α in this case) exhibits *miscibility gap*, such as shown in Figure 10.17, in which case the material phase separates. The schematic curve shown in Fig.10.17 shows two minima, near compositions x_1 and x_2.
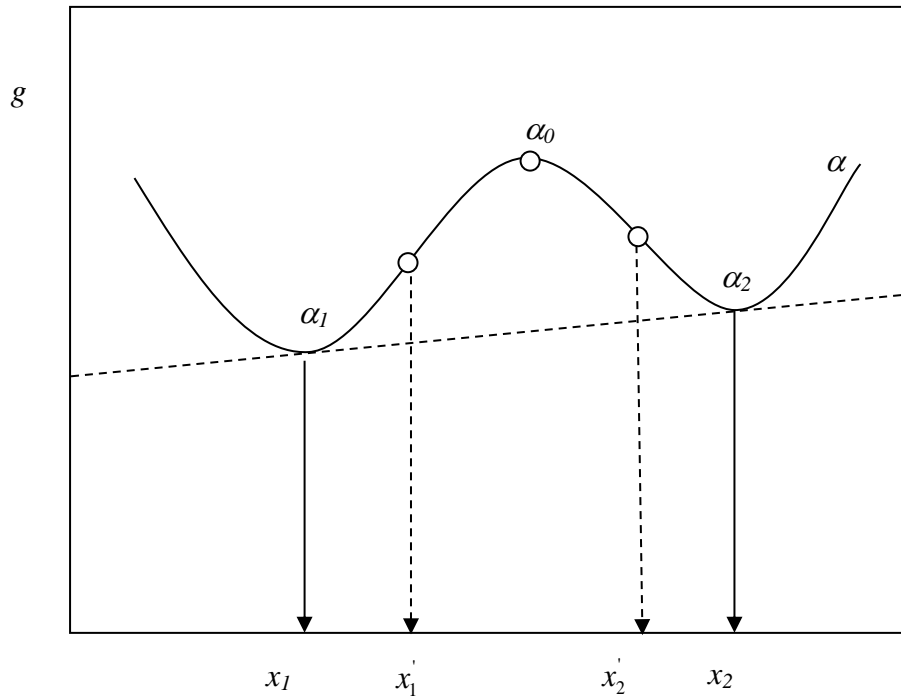
Figure 10 17 : Schematic of the spinodal decomposition process

For any point in the region between x_1 and x_2, an argument analogous to that shown in section 10.2.2, can be used to show that it is energetically favorable for the alloy to

separate into two regions with compositions x_1 and x_2. In particular for a phase with composition α_o the following reaction is favorable:

$$\alpha_o \rightarrow \alpha_1 + \alpha_2 \tag{10.50}$$

Note that the curve between x_1 and x_2 has at first a *positive* second derivative and then, at point x_1, the second derivative becomes *negative*. Where the second derivative is negative, spinodal decomposition occurs without a nucleation barrier, since the overall Gibbs energy is reduced, by a similar argument as in 10.2.2. When the second derivative is positive, a barrier exists for phase separation that requires nucleation of the second phase to achieve decomposition.

10.4.5 Precipitate loss of coherency

As the second phase precipitate forms it normally starts out coherent with the matrix, i.e., there is an orientation relationship between the planes of the precipitate and the planes of the matrix atoms, such that lattice matching occurs across the interface. This is another way (in addition to heterogeneous nucleation) to minimize surface energy, and make the transformation easier, although with a cost in elastic strain energy. As the precipitate grows it eventually loses coherency with the matrix, that is, no longer does a matching of atoms occur across the interface, and as a result the interfacial energy increases. This, however, allows the elastic strain energy to be minimized and this is a more important term for larger precipitates.

10.4.6 Precipitate coarsening-Ostwald Ripening

Once precipitates have lost coherency with the matrix and a precipitate size distribution is established in equilibrium with the matrix, the precipitate size distribution can still evolve as a "zero-sum game" in which some precipitates shrink while others grow. This redistribution of atoms occurs because of higher interface energies of small particles with large surface-to-volume ratios which cause larger precipitates to grow at the expense of smaller ones.

For a given precipitate volume fraction a smaller number of larger precipitates results in an overall smaller surface area and thus reduces the energy of the system. For example, for a total precipitate volume V_p, compare the surface areas if all the volume is in a single precipitate which would mean a precipitate volume of $4\pi R^3/3$ [$R= (3V/4\pi)^{1/3}$]

$$SA_1 = 4\pi R^2 = (4\pi)^{1/3}(3V)^{2/3} \tag{10.51}$$

If this volume was instead divided into N_p precipitates of equal volume the precipitate volume would be

$$V / N_p = 4\pi R_p^{\ 3} / 3N_p \quad \therefore \quad R_p = (3V / 4\pi N_p)^{1/3} \tag{10.52}$$

and the surface area would be

$$SA_{N_p} = 4\pi N_p \left(3V / 4\pi N_p\right)^{2/3} = (4\pi)^{1/3}(3V)^{2/3}N_p^{1/3} = (SA_1)N_p^{1/3} \tag{10.53}$$

Thus the surface area increases with increasing N_p and there is a driving force to reduce the overall surface area by increasing the average precipitate size.

The process by which this redistribution occurs is the so-called *Ostwald ripening* process and involves the transfer of atoms from small to large precipitates. This process leads to a cubic coarsening rate law, as is shown in the following derivation, adapted from [5, 6].

Consider a distribution of precipitates of various sizes, in a situation where the concentration of solute in solid solution is equal to the equilibrium concentration. Once precipitation ends, the precipitate volume fraction remains essentially constant, in equilibrium with an average solute content in the beta matrix, c^{eq}. In this scenario only the precipitate size distribution changes, causing the average precipitate size to increase. In that case

$$\sum_i \frac{dn_i}{dt} = 0 \tag{10.54}$$

where n_i is the number of atoms in precipitate i and the sum is performed over all precipitates. If the atomic volume is Ω then for spherical precipitates

$$\sum_{i=1,...N} \frac{1}{\Omega}\frac{dV_i}{dt} = \sum_{i=1,...N} \frac{4\pi r_i^2}{\Omega}\frac{dr_i}{dt} = 0 \tag{10.55}$$

where r_i is the particle radius and N is the total number of particles. The growth of the precipitate can be controlled by either solute diffusion or surface reaction. Since the latter is normally fast compared to the former, it is assumed that precipitate growth is diffusion controlled. In that case the diffusion controlled atom flux leaving the particle is given by

$$J = 4\pi r_i^2 (-D)\left(\frac{dc}{dr}\right)_{\alpha S} \tag{10.56}$$

where D is the diffusion coefficient, r is the radial coordinate and c is the concentration (atom.m^{-3}), and the derivative is calculated at the alpha precipitate surface S. The concentration at the curved surface c_S is enhanced relative to that at a flat surface, c_f because, as predicted by the Gibbs-Thomson equation [4]

$$c_S = c_f \left[1 + \frac{2\Omega\gamma}{r_i k_B T}\right] \tag{10.57}$$

where Ω is the surface energy. The radial solute concentration gradient at the surface of a sphere of radius r_i is

$$\left(\frac{dc}{dr}\right)_{\alpha S} = \frac{c_S - c^{eq}}{r_i} \tag{10.58}$$

where c^{eq} is the concentration far from the precipitate. Combining (10.58) and (10.56) and setting that equal to equation (10.55) written for a single particle

$$\frac{dr_i}{dt} = \frac{-\Omega D(c_S - c^{eq})}{r_i} \tag{10.59}$$

Substituting (10.59) into (10.55)

$$(c_S - c^{eq})\sum_i r_i = Nc_f \frac{2\Omega\gamma}{k_B T} \tag{10.60}$$

Noting that $\bar{r} = \dfrac{\sum_i r_i}{N}$

$$(c^{eq} - c_S) = \frac{2\Omega\gamma}{k_B T}c_f\left(\frac{1}{\bar{r}} - \frac{1}{r_i}\right) \tag{10.61}$$

Substituting equation (10.61) into (10.59)

$$\frac{dr_i}{dt} = \frac{2\Omega^2\gamma Dc_f}{k_B T r_i^2}\left[\frac{r_i}{\bar{r}} - 1\right] \tag{10.62}$$

Note that this equation indicates precipitate growth when $r_i > \bar{r}$ and shrinkage when it is smaller. Integrating and solving for the maximum radius

$$r_{max}^3 - r_o^3 = 6\frac{2\Omega^2\gamma c_f D}{k_B T}t \tag{10.63}$$

Wagner and Lifshitz using a more sophisticated theory were able to derive the evolution of the mean particle size as [7, 8]

$$\bar{r}^3 - \bar{r}_o^3 = \frac{8}{9}\frac{\Omega^2\gamma c_f D}{k_B T}t \tag{10.64}$$

Equation (10.64) shows that a precipitate will coarsen according to cubic kinetics.

10.5. Diffusionless Phase Transformations: Martensitic transformation

At the other extreme from diffusion-controlled transformations are *diffusionless* phase transformations. In contrast with the diffusion-controlled (or replacive) transformations, diffusionless transformations (also called displacive) require no long-range transport of chemical species and thus can occur relatively quickly. Such transformations are also called *martensitic transformations* in honor of A. Martens who described them in steels. These transformations are technologically important and include the austenite to martensite transformation in steels and the monoclinic-to-tetragonal transformation in ZrO_2 layers formed during zirconium alloy corrosion.

Consider and Fe 0.4%C alloy being held in the single phase austenite (γ-Fe) field (say, at 1000 C in Fig.10.5 (h)) that is suddenly quenched (cooled rapidly by immersion in a liquid , oil for example). Although the stable phase equilibrium would be a combination of iron and Fe_3C carbide (called cementite) the phase observed upon rapid cooling is called martensite. Martensite is a supersaturated solid solution of carbon in a α-Fe (bcc-Fe or ferrite) which the carbon interstitials actually distort into a body centered tetragonal structure. The high rate of cooling involved in quenching does not allow enough time for the atoms to come out of solution, which would permit decomposition into ferrite and cementite (Fe_3C). Thus, martensite is a *metastable* phase and, by definition, it does not appear in the Fe-C equilibrium phase diagram. Because carbon is an austenite-stabilizing element, some austenite is retained upon quenching when the concentration of carbon is solid solution is high.

The effect of martensite formation with its high carbon supersaturation is to increase the hardness of the material and to make it more brittle. The degree of hardening depends on the amount of C. As a result, tempering heat treatments are normally conducted to allow the carbon to partially come out of solution and form cementite. As this occurs, the material becomes less hard and more ductile because the carbon gradually forms carbides and approaches phase equilibrium. By varying the heat treatment, different degrees of transformation and thus different levels of hardening and ductility can be achieved.

The martensitic transformation has been the object of much still-ongoing study. It is beyond the scope of this text to analyze the detailed transformation mechanisms which have been discussed elsewhere [3, 9]. It is clear however that this transformation occurs without change in chemical composition and by small atomic displacements within the unit cell. These atomic motions occur in a coordinated fashion so that the ensemble of atoms moves together in lock step. Because these transformations involve regimented atomic rearrangements they have also been called *military* transformations, in contrast to the relatively disordered thermally-activated nucleation and growth processes (also called *civilian* transformations). Finally because no diffusion occurs, such atomic movements have to take place by athermal processes such as twinning or dislocation motion (see Chapter 11).

10.6. Order-Disorder Transformations

Phase transformations in alloys can further be classified by whether they are *clustering* or *ordering*, that is, whether it is more favorable to form A-B bonds than A-A and B-B bonds. In many metal alloys, ordering is not important – in other words the bonding energy between different pairs of atoms differ little from each other. In other compounds, such as the intermetallic compounds seen as precipitates in Zr alloys the order is so important that they only form in near stoichiometric compositions to maximize the ability to form unlike bonds.

For nuclear materials, when subjected to irradiation some of the atom pairs may be mixed by the energetic particles, which would cause these compounds to be less stable and either amorphize or dissolve, as discussed in Chapter 24.

The tendency to form unlike or like bonds (or to be indifferent) is measured by the *ordering energy w*:

$$w = \varphi_{AB} - \frac{\varphi_{AA} + \varphi_{BB}}{2}$$ (10.65)

where φ_{ij} is the bond energy of the *ij* pair. When $w > 0$, clustering is favored, and when $w < 0$, ordering is favored.

For example in Figure 10.xx (a) the lattice is completely ordered as AB bonds are favored, while in Fig. 10.xx (b) the

| (a) | (b) | (c) |
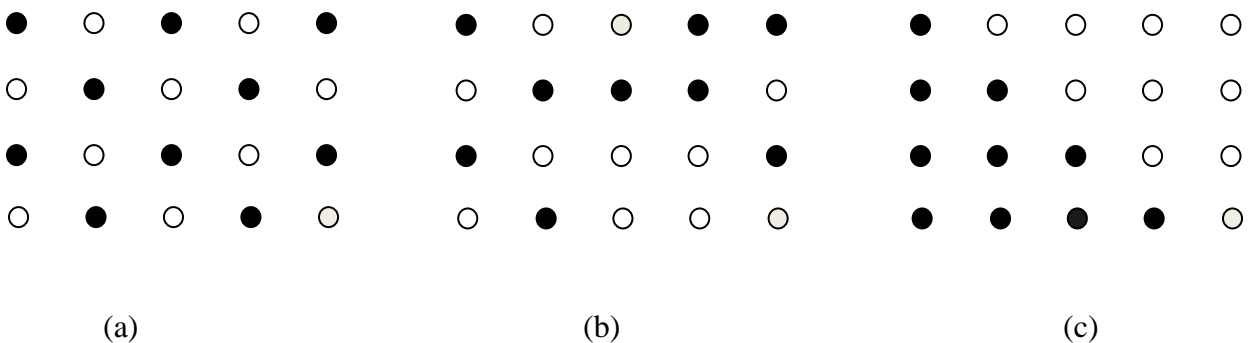
Figure 10.19 (a) w <0 Ordering, (b) w ~0, disordering and (c) w>0, clustering

An ordered compound has at least two sub-lattices, each occupied by different chemical species. The degree of order in such materials can be measured by the long-range order parameter *S* and the short-range order parameter σ. The former is given by

$$S = \frac{P_{aa} - x_a}{1 - x_a} \qquad (10.66)$$

where P_{aa} is the probability of finding an atom of type "a" on an "a" sublattice site, and x_a is the mole fraction of a in the alloy. In a perfectly ordered compound, the probability of finding an "a" atom in an "a" site is 100% so $P_{aa}=1$ and $S=1$. In a perfectly disordered compound, the probability of finding an "a" atom at an "a" site is purely random (i.e. the atoms are evenly mixed in the lattice) and thus $P_{aa} = x_a$, so that S=0.

The short-range order parameter is given by

$$\sigma = \frac{N_{ab} - N_{ab}^{dis}}{N_{ab}^{ord} - N_{ab}^{dis}} \qquad (10.67)$$

where N_{ab} is the number of *a-b* pairs in the compound, N_{ab}^{dis} is the number of *a-b* pairs in the perfectly disordered compound, and N_{ab}^{ord} is the number of *a-b* pairs in the perfectly ordered compound, resulting again in an order parameter of $\sigma =1$ for a perfectly ordered material and $\sigma =0$ for perfectly disordered material.

Both parameters describe the state of chemical order of the material, but in general the long-range order parameter is more-easily accessible experimentally. The classical means of detecting long-range order is by the presence of superlattice reflections (see below) which are extinguished when the long-range order parameter goes to zero.
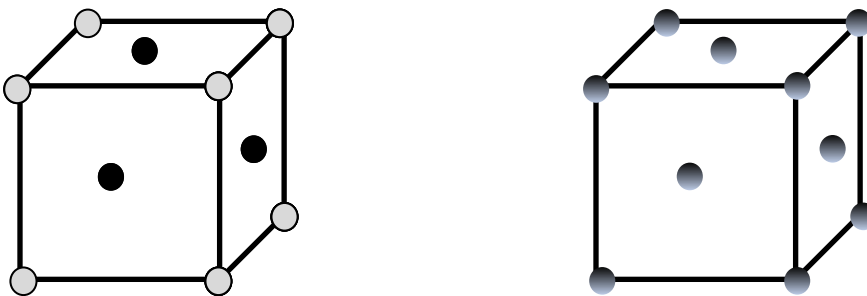
Figure 10.20. The structure of Cu₃Au. The ordered structure (a) is a simple cubic arrangement while the disordered structure (b) constitutes a fcc lattice. The Au atoms (light-colored) occupy a simple-cubic lattice on the corners with the Cu atoms (dark) on each face.

Figure 10.20 shows a unit cell of Cu₃Au. When the compound is fully ordered, only Cu atoms are found on Cu sites, and only Au atoms on gold sites. When the compound is

fully disordered the probability of finding atoms in particular lattice positions is given by the compound stoichiometry. Thus the crystal structure changes symmetry from simple cubic with a basis of 4 (3Cu and 1 Au) to fcc with an average atom in each site. The particular atomic arrangement of the fcc lattice causes diffraction from some sets of planes to interfere destructively, and so some reflections are not allowed (see Chapter 3). For example, when the (100) planes are at the exact Bragg condition for reinforcement from successive planes, there is a plane in between with the same atom density and which, by virtue of being midway between successive 100 planes, interferes destructively and causes a diffraction *extinction*[10]. This does not occur in the simple cubic structure, and thus as the material goes from disordered to ordered, many new (superlattice) reflections appear which can be used to monitor the degree of order.

We should note that following the evolution of the parameter *S* from superlattice reflections is only possible in materials that change symmetry upon disordering as do the Cu_3Au (simple cubic to face centered cubic) or CsCl structures (simple cubic to body centered cubic). To detect the changes in short-range order is a more complicated task. Furthermore, it is possible to have almost no long-range order, but still a great deal of short-range order as described in Example # 1.

Example # 1 Relationship between S and σ
For a two-sublattice ordered crystal the short-range order parameter corresponding to a long-range order parameter is calculated below.

The number of *a-b* atom pairs in a crystal per sub-lattice site is given by

$$N_{ab} = P_{aa}P_{bb}Z + P_{ba}\ P_{ab}Z \tag{10.68}$$

where *Z* is the number of nearest neighbors and the P_{xy} is the probability of finding atom x on sublattice y. From Eq (10.66), these are:

$$P_{aa} = x_a + S(1-x_a); P_{ba} = 1 - P_{aa}$$
$$P_{bb} = x_b + S(1-x_b); P_{ab} = 1 - P_{bb} \tag{10.69}$$

substituting Eqs (10.69) into (10.68) and rearranging yields:

$$N_{ab} = 2Z\left[x_a(1-x_a)S^2 + \frac{(2x_a-1)^2}{2}S + x_a(1-x_a)\right] \tag{10.70}$$

For two sublattices with $x_a=0.5$, this reduces to

$$N_{ab} = 2Z\left[\frac{1}{4}S^2 + \frac{1}{4}\right] \tag{10.71}$$

The extreme cases are when *S=1* and *S=0*. According to the formula above, for *S=1* (perfect order) the number of pairs per lattice site is *Z*, as expected. For *S=0*, the number of *a-b* pairs per

lattice site is *Z/2*, also as expected since in the case of random distribution of atoms in the sublattices in an equiatomic compound there is an equal chance of finding either a or b atoms and thus the number of pairs is reduced by half.

Returning to equation (10.71), we can now write N_{ab}^{ord} and N_{ab}^{dis} and , the number of ab pairs is:.

For S=1

$$N_{ab}^{ord} = Z \tag{10.72}$$

For *S=0*

$$N_{ab}^{dis} = 2Zx_a(1-x_a) \tag{10.73}$$

Substituting equations (10.71)(10.72)and (10.73) into (10.67) the short-range order parameter for a two-sublattice compound is:

$$\sigma = \frac{Z\left[2x_a(1-x_a)S^2 + (2x_a-1)^2 S + 2x_a(1-x_a)\right] - 2(x_a(1-x_a))Z}{1-2(x_a(1-x_a))Z} \tag{10.74}$$

Equation (10.74) gives the lower bound of the degree of short-range order that would be expected from a given degree of long-range order.
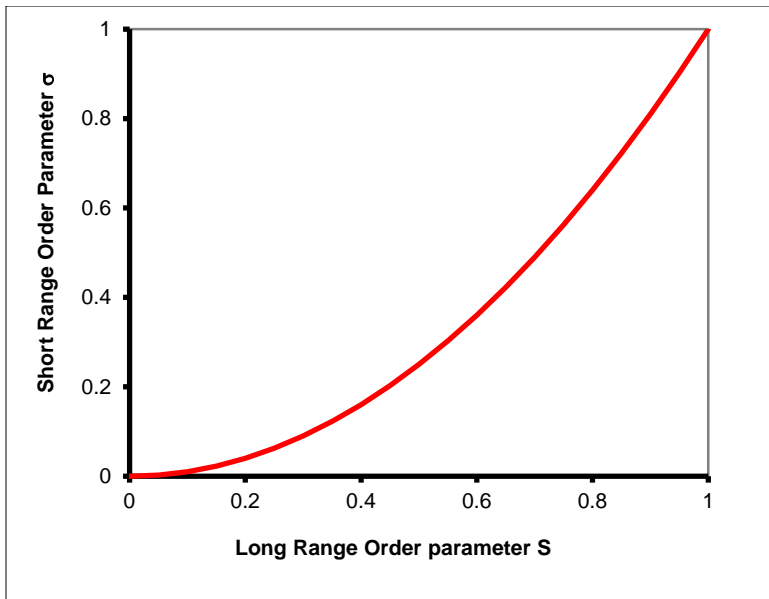

Figure 10.21: Relationship between the long-range and short range order parameters.

This shows that order can be characterized by two different but related parameters.

10.7 Amorphization

Although long-range order is absent in a liquid, there is some degree of short-range order. Normally, a liquid is stable at temperatures where the entropic contribution to the Gibbs energy increases the stability of structures with high degrees of disorder. Although the Gibbs energy of an ordered crystalline solid is intrinsically lower than that of an amorphous solid (no topological order) or of a chemically-disordered solid (no chemical long-range order), metastable disordered or *amorphous* solids exist when the stable crystalline configuration is kinetically inaccessible. One common example is the formation of an amorphous solid upon very fast cooling from the melt. If the cooling rate is fast enough, short-range order may be established during cooling, with no topological order, which creates an amorphous solid. This is why amorphous solids are often referred by the contradictory term "frozen liquid".

Quantitatively, the degree of order of crystalline solids can be described by the *radial distribution function*, *g(r)*. This function describes the probability of finding another atom at a given distance from a particular atom. Figure 10.22 shows an example of *g(r)* for a crystal and for a liquid. In the latter, as in an amorphous solid, although a well-defined relationship to their first nearest neighbors exists, (as shown by the large first peak), this correlation decreases with distance such that there is only a wide peak in the second nearest-neighbor distance, decreasing to a random probability thereafter. In the crystal, although the peak heights decrease with distance because of the above factors, the correlation distance is much greater than in the amorphous solid.

In an *ideal* crystal at 0 K, the probability of finding an atom at one of the lattice positions is unity. In a real crystal, lattice imperfections, such as point defects, dislocations, and grain boundaries, destroy the correlation that exists between lattice positions in a perfect crystal. As a result, the interatomic distances vary, and these variations increase with distance such that the interatomic correlations decrease with distance.
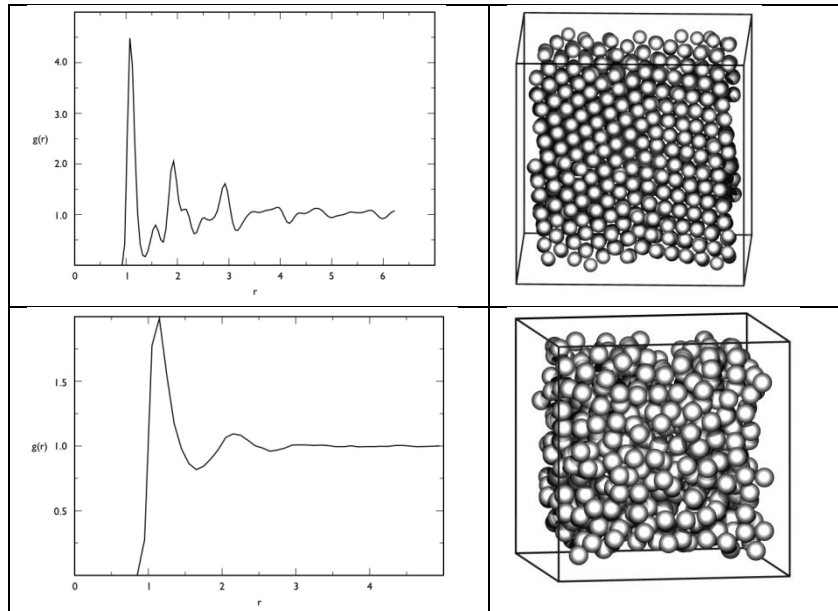
Figure 10.22: The x-ray diffraction radial distribution functions g(r) plotted versus r for a solid (top) and a liquid (bottom) (courtesy of C. Iacovelli and S.Glotzer, University of Michigan)

Besides fast quenching, a metastable amorphous phase can form during other non-equilibrium processes. Irradiation can also make crystalline phases amorphous and cause chemically-ordered phases to become disordered, as discussed in Chapter 24. Amorphization comes as a response of the materials to reduce long range order while maintaining short range order. Because of the volume expansion and loss of stability associated with the transformation amorphization should be avoided, normally by operating the material at a temperature enough to dynamically anneal the material during irradiation

Problems

10.1. Describe qualitatively what would occur to a melt of Zr-10%Cr as it is slowly cooled from 1750 °C down to 700 °C, in quasi-equilibrium. Describe what phases would appear, their compositions and how the volume fractions and compositions of these phases would change as the temperature is steadily decreased. Do a neat sketch with illustrations at important points in the process to help convey the physical processes taking place taking special attention to the regions where phase transformations take place.

10.2. Using the Zr-Cr phase diagram shown in the Figure 10.5 answer the questions

a. For a solid containing 22 atom %Cr, and at equilibrium at T=1330 °C, identify the phases present, their relative amounts (how much of each phase is present) and their composition (Cr atom % for each).
b. The maximum solubility of Cr (atom %Cr) in the beta phase of Zr and the temperature at which it occurs. At 1100 °C, what occurs when the solubility limit of Cr in the beta phase is reached?
c. Construct Gibbs energy curves for T = 400 °C , 1100 °C, and 1650 °C that are consistent with the Zr-Cr phase diagram given in the notes. Indicate the phases associated with each curve, in each case.
d. For a 60 at% Cr, 40 at % Zr mixture at 1100 °C at equilibrium, what phases are present, in what composition and in which proportions?
e. Calculate the maximum possible equilibrium vacancy concentration in pure beta Zr, if the vacancy formation energy is 1.6 eV (5).

10.3. For the 2D figure below, calculate the long range S and short range order parameter σ. Use Z=4 and consider only the atoms which have all 4 nearest neighbors
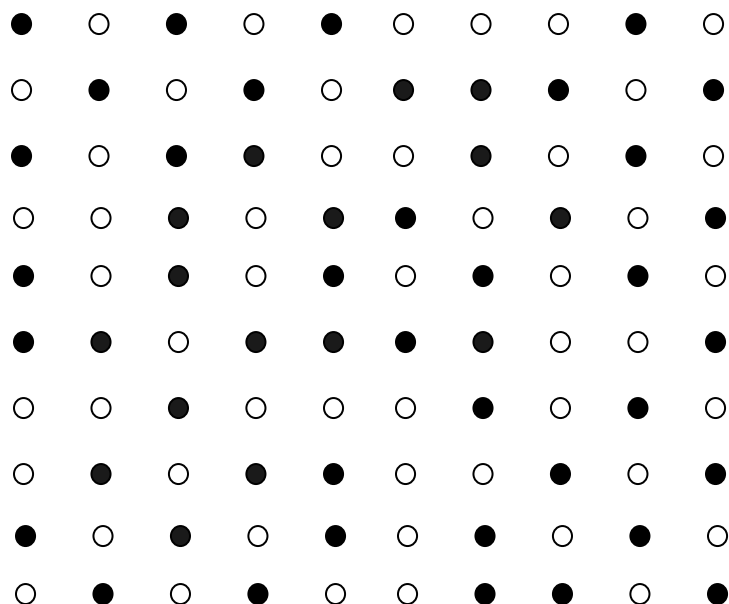
b) How many atoms would have to be moved for perfect order (both S and σ) to be established?

10.4. During cooling from high temperature a second phase "beta" precipitates from a solid solution in the "alpha" phase.

a) If the precipitate is spherical radius r, and the surface energy of the alpha-beta interface is 1 J/m^2 and the change in Gibbs energy from beta to alpha is 23 KJ/mol calculate the critical radius at the transformation temperature, if the material density is 7 g/cm^3. What would likely occur to the critical radius if the temperature were further decreased below the precipitation temperature? Why?

b) Assume now that the precipitate is plate-like with a thickness and that the surface energy of the plate surface is xΩ, where x is a number between 0 and 1. Estimate the plate dimensions as a function of x. Assume that the two in-plane directions are equivalent and that elastic forces play no role in the transformation.

References

[1] P. J. Spencer, "A Brief History of CALPHAD," *Calphad-Computer Coupling Of Phase Diagrams And Thermochemistry*, vol. 32, pp. 1-8, 2008.
[2] M. Volmer, *Z. Elektrochem.*, vol. 35, pp. 55, 1929.
[3] J. W. Christian, *The Theory of Transformations in Metals and Alloys, part I: Equilibrium and General Kinetic Theory, 2nd edition*. Oxford: Pergamon Press, 1975.
[4] D. A. Porter and K. E. Easterling, *Phase Transformations in Metal and Alloys*, 2nd ed. London: Chapman and Hall, 1993.
[5] J. Verhoeven, *Fundamentals of Physical Metallurgy*. New York: Wiley and sons, 1975.
[6] G. W. Greenwood, in *The Mechanism of Phase Transformations in Crystalline Solids,* , J.W.Cahn, Ed. London, 1969, pp. 103-110.
[7] J. M. Lifshiz and V. V. Slyozov, *Journal of Physical Chemistry of Solids*, vol. 19, pp. 35, 1961.
[8] C. Wagner, *Zeitshrift fur Elektrochem.*, vol. 65, pp. 581, 1961.
[9] H. K. D. H. Bhadeshia, "Martensitic Transformation," in *Encyclopedia of Materials Science: Science and Technology*, R. W. C. K. Buschow, M. C. Flemings, B. Iischner, E. J. Kramer and S. Mahajan, Ed.: Pergamon Press, Elsevier Science, 2001, pp. 5203-5206.
[10] B. D. Cullity, *Elements of X-ray Diffraction*. Reading, MA: Addison-Wesley, 1978.